Numerička simulacija procesa spreja i izgaranja

Jurić, Filip

UNIVERSITY OF ZAGREB
FACULTY OF MECHANICAL ENGINEERING AND NAVAL ARCHITECTURE

MASTER'S THESIS

Filip Jurić

Zagreb, 2016.

UNIVERSITY OF ZAGREB
FACULTY OF MECHANICAL ENGINEERING AND NAVAL ARCHITECTURE

NUMERICAL MODELLING OF SPRAY AND COMBUSTION PROCESS

Supervisor:

Asst. Prof. Milan Vujanović, PhD

Student:

Filip Jurić

Zagreb, 2016.

I hereby declare that this thesis is entirely the result of my own work except where otherwise indicated. I have fully cited all used sources, and I have only used the ones given in the list of references.

I am truly thankful to Professor Milan Vujanović for being the supervisor of the thesis. His supervision has always been very helpful and patience.

Special thanks to project assistant Dr. Zvonimir Petranović whose guidance, knowledge, insights, help, support and advice significantly contributed to the work presented in the thesis.

I would like to express my gratitude to Professor Tomaž Katrašnik and his assistant Rok Vihar for a nice hospitality in Ljubljana and provided experimental data.

I would also like to acknowledge the financial support of Adria Section of the Combustion Institute (ASCI).

Also, I need to thank all the people who create such a good atmosphere at the PowerLab CFD office; Dr. Jakov Baleta, Dr. Hrvoje Mikulčić, Dr. Marko Ban and Tibor Bešenić

Last but not least, I would like to thank my parents for their patience, understanding and great support.

Filip Jurić

SVEUČILIŠTE U ZAGREBU
FAKULTET STROJARSTVA I BRODOGRADNJE
Središnje povjerenstvo za završne i diplomske ispite
Povjerenstvo za diplomske ispite studija strojarstva za smjerove:
procesno-energetski, konstrukcijski, brodostrojarski i inženjersko modeliranje i računalne simulacije

Sveučilište u Zagrebu Fakultet strojarstva i brodogradnje	
Datum	Prilog
Klasa:	
Ur.broj:	

DIPLOMSKI ZADATAK

Student: **Filip Jurić** Mat. br.: 0035187476

Naslov rada na hrvatskom jeziku: **Numerička simulacija procesa spreja i izgaranja**

Naslov rada na engleskom jeziku: **Numerical modelling of spray and combustion processes**

Opis zadatka:

Korištenje računalne dinamike fluida (RDF) u kombinaciji s eksperimentalnim pristupom postao je uobičajen pristup u razvoju različitih inženjerskih sustava. Uslijed utjecaja inercije, površinske napetosti i aerodinamičkih sila dolazi do raspadanja goriva na sitne kapljice, njihovog isparavanja te miješanja sa smjesom plinova. Opisani proces, koji se naziva sprej, ima utjecaj na efikasnost sustava koja se može povećati optimiranjem relevantnih matematičkih modela. Prilikom rada motora s unutarnjim izgaranjem, uslijed takta kompresije, dolazi do povećanja tlaka i temperature smjese plinova te do zapaljenja gorivih para. U okviru diplomskog zadatka potrebno je:

1. Opisati osnovne jednadžbe računalne dinamike fluida te opisati jednadžbe korištene za opisivanje procesa spreja i procesa izgaranja;
2. Prikazati numeričke metode koje će se koristiti za rješavanje problema;
3. Računalno modelirati proces ubrizgavanja i proces izgaranja;
4. Modelirane rezultate usporediti s dostupnim eksperimentalnim podacima. Sva literatura, modeli te ulazni i početni podaci za analizu slučaja bit će dostupni od strane mentora i neposrednog voditelja.

Zadatak zadan:	Rok predaje rada:	Predviđeni datumi obrane:
29. rujna 2016.	1. prosinca 2016.	7., 8. i 9. prosinca 2016.

Zadatak zadao: Predsjednica Povjerenstva:

Doc. dr. sc. Milan Vujanović Prof. dr. sc. Tanja Jurčević Lulić

TABLE OF CONTENTS

LIST OF FIGURES

LIST OF TABLE

NOMENCLATURE

Latin	**Description**	**Unit**
A	Constant in Arrhenius law	
c	Concentration	kgm^{-3}
C	Model coefficient	
D	Droplet diameter	m
D_k	Diffusion coefficient	m^2s^{-1}
e	Specific energy	Jkg^{-1}
E_a	Activation energy	Jkg^{-1}
f_r	Frequency	Hz
f	Fuel mass fraction	
F_d	Drag force	N
g	Mass fraction of gas residuals	
h	Enthalpy	$kJ(kg)^{-1}$
k	Turbulent kinetic energy	m^2s^{-2}
k_k	Global reaction rate coefficient	
L	Turbulence length scale	m
m	Mass	kg
M	Molar mass	$kg(kmol)^{-1}$
p	Pressure	Pa
P	Production of turbulent kinetic energy	W
q	Specific heat	Wkg^{-1}
r	Droplet radius	m
R	Ideal gas constant	$J(molK)^{-1}$
S	Source of extensive property	
S	Surface	m^2
t	Time	s
T	Turbulence time scale	s
T	Temperature	K
u	Velocity	ms^{-1}
V	Volume	m^3

x_i	Cartesian coordinates	m
y	Mass fraction	

Greek	**Description**	**Unit**
β	Coefficient in Arrhenius law	
Γ	Diffusion coefficient	
δ	Kronecker delta	
ε	Turbulent kinetic dissipation rate	m
ζ	Normalised velocity scale	
λ	Thermal conductivity coefficient	$W(mK)^{-1}$
λ_w	Wavelength	m
μ	Dynamic viscosity	Pas
μ_t	Turbulent viscosity	Pas
ρ	Density	kgm^{-3}
σ	Surface tension	Nm^{-1}
σ_{ij}	Stress tensor	Nm^{-2}
τ	Viscous stress	Nm^{-2}
τ_a	Breakup time	s
υ	Kinetic viscosity	m^2s^{-1}
φ	Extensive property of general conservation equation	
ω	Combustion source	
Ω	Wave growth rate	s

Dimensionless quantity

Le	Lewis number
Nu	Nusselt number
Pr	Prandtl number
Re	Reynolds number
Oh	Ohnesorge number
Sc	Schmidt number
Ta	Taylor number
We	Weber number

Abbreviations

2D	Two-Dimensional
3D	Three-Dimensional
BDC	Bottom Dead Centre
CA	Crank-Angle
CFD	Computational Fluid Dynamics
CI	Compression Ignition
DDM	Discrete Droplet Method
DI	Direct Injection
EGR	Exhaust Gas Recirculation
FVM	Finite Volume Method
MI	Main Injection
PI	Pilot Injection
RANS	Reynolds Averaged Navier-Stokes
TDC	Top Dead Centre

ABSTRACT

Using CFD in combination with experimental research has become a standard approach in the development of Diesel engines. In this work, the numerical simulation of Diesel engine combustion process with the commercial 3D Computational Fluid Dynamics (CFD) software AVL FIRE® is compared with the experimental data. The experimental data was provided by collaboration with the Faculty of Mechanical Engineering, the University of Ljubljana. Characteristic for the observed experimental Diesel engine is that the liquid fuel is injected through the pilot and main injections. The pilot injection is used to produce an amount of vapour that later ignites, and increases the mean in-cylinder temperature. At later crank angle positions the main injection occurs. The comparison between modelling results obtained with the combustion model ECFM 3Z+ and chemical mechanism is shown. Furthermore, an investigation of the calculated and the experimental data for two different engine operating points is presented. The results from numerical simulations, such as the mean pressure, mean temperature, and the rate of heat release are found to be in agreement with the experimental data.

Keywords: Spray, Diesel engine, Euler Lagrangian, multi-injection

SAŽETAK

Korištenje Računalne Dinamike Fluida (RDF) u kombinaciji s eksperimentalnim istraživanjem postalo je uobičajeni pristup u razvijanju dizel motora. U ovom radu je prikazana usporedba rezultata numeričke simulacija izgaranja u dizel motoru koristeći komercijalni programski paket AVL FIRE® s eksperimentalnim podacima. Eksperimentalni podaci su dobiveni u suradnji s Fakultetom Strojarstva, Sveučilišta u Ljubljani. Karakteristično za promatrani eksperimentalni dizel motor je pojedinačno ubrizgavanje goriva u pred ubrizgavanju i u glavnom ubrizgavanju. Izgaranjem relativno male količine isparenog goriva ubrizganog u pred ubrizgavanju postiže se viši tlak unutar cilindra prije glavnog ubrizgavanja. Glavno ubrizgavanje počinje u trenutku kad je klip u blizini gornje mrtve točke. U ovom radu također je prikazan usporedba između modela izgaranja ECFM 3Z+ i kemijskog mehanizma. Na kraju je prikazana analiza eksperimentalnih podataka i rezultata simulacija za dva radna stanja motora. Rezultati tlaka i temperature u cilindru te brzina oslobođene topline dobivena iz numeričkih simulacija prikazuju dobro poklapanje s eksperimentalnim podacima.

Ključne riječi: Sprej, dizel motor, Euler Lagrange, pojedinačno ubrizgavanje

PROŠIRENI SAŽETAK

(EXTENDEND ABSTRACT IN CROATIAN)

UVOD

Poznato je da 93 % ukupne energije potrošene u transportu potječe iz fosilnih goriva, što transportni sektor čini najmanje raznolikim [1]. Trenutno, u Europi je potrošnja dizel goriva 2.6 puta veća nego potrošnja benzinskog goriva, i ta razlika još je u porastu [1]. Kvaliteta procesa spreja u dizel motorima utječe na efikasnost rada motora, stoga je nužno razvijati i optimizirati matematičke modele koji se koriste za opisivanje tog procesa.

Korištenje računalne dinamike fluida značajno smanjuje vrijeme i troškove razvoja dizel motora. U dizel motorima RDF simulacije se koriste za istraživanje utjecaja turbulencije, goriva, procesa spreja i izgaranja na cjelokupni rad motora. Dobiveni rezultati temperaturnog polja, spreja, isparenog goriva, procesa izgaranja, itd., kasnije se mogu koristiti u poboljšanju konstrukcije i efikasnosti motora.

MATEMATIČKI MODEL

U ovom radu proces spreja opisan Euler Lagrange pristupom, koji tekuću fazu goriva računa kao Lagrangeove parcele, gdje je koordinatni sustav vezan na parcele. Plinovita faza smatra se kontinuumom, te su za nju rješavane jednadžbe očuvanja (Euler pristup). Jednadžbe očuvanja mogu se prikazati općenitom jednadžbom očuvanja:

$$\int_V \frac{\partial}{\partial t}(\rho\,\varphi)\,dV + \int_S \rho\,\varphi\,u_i\,n_i\,dS = \int_S \Gamma_\varphi\,\frac{\partial \varphi}{\partial x_i} n_i\,dS + \int_V S_\varphi dV \qquad (1)$$

Nestacionarni član | Konvekcija | Difuzija | Izvor/Ponor

gdje se zamjenom oznake φ s fizikalnom veličinom definiranom u Tablici 1. dobiva željeni zakon očuvanja.

Tablica 1. Fizikalne veličine zakona očuvanja

Zakon očuvanja:	Fizikalna veličina, φ
Ukupne mase	ρ
Momenta	ρu_i
Energije	ρe
Mase komponente	y_k

Modeliranje turbulencije

Turbulentno strujanje postoji u skoro svim inženjerskim sustavima, stoga je za rješavanje problema potrebno koristiti modele turbulencije koji aproksimiraju stvarno strujanje. Modeli turbulencije aproksimiraju tenzor turbulentnih naprezanja. U ovom radu korišten je k-zeta-f model turbulencije koji je implementiran u programski paket AVL FIRE®.

Modeliranje spreja

U ovom radu sprej je modeliran Euler Lagrangian pristupom u kojem se kapljice kapljevitog goriva podijeljene u parcele čije se trajektorije prate kroz računalnu domenu. Isparavanjem parcela i izgaranjem isparenog goriva oslobađa se toplina koja se modelira kao izvor u jednadžbi o očuvanju energije. Sila otpora je sila koja ima najveći utjecaj na gibanje parcele. Trajektorija parcela dobiva se integriranjem ubrzanja dobivene iz 2. Newtonovog zakona:

$$m_\mathrm{p} \frac{du_{\mathrm{p}i}}{dt} = F_{\mathrm{d}i} \tag{2}$$

$$x_{\mathrm{p}i}(t) = \int_t^{t+\Delta t} u_{\mathrm{p}i}\, dt \tag{3}$$

gdje je m_p masa parcele, $u_{\mathrm{p}i}$ brzina parcele, a $F_{\mathrm{d}i}$ sila otpora na gibanje parcele.

U ovom radu korišteni su slijedeći pod modeli spreja:

- Model raspadanja čestica → WAVE
- Model isparavanja → Dukowicz
- Model sile otpora → Schiller-Naumann
- Model međudjelovanja sa stjenkama → Walljet1

Model raspadanja čestica WAVE

Povećanje perturbacije na površini parcele je u ovisnosti s vlastitom valnom duljinom. Konstanta WAVE modela C_2 služi za kalibraciju modela spreja za pojedini tip sapnice. Konstanta C_2 definira vrijeme raspadanja kapljica koje je opisano jednadžbom:

$$\tau_a = \frac{3.726\ C_2\ r}{\lambda_w\ \Omega} \tag{4}$$

gdje je r radijus kapljice, λ_w valna duljina perturbacija i Ω brzina rasta valova perturbacije. Povećanjem koeficijenta C_2, vrijeme raspadanja kapljica je duže.

Modeliranje izgaranja

U ovome radu proces izgaranja modeliran je na dva različita načina:

- Kemijski mehanizam
- Model izgaranja

U kemijskom mehanizmu se za sve kemijske vrste računaju transportne jednadžbe (zakon o očuvanju mase kemijske vrste). Izvorski član u jednadžbi o očuvanju energije za izvorski član se modelira pomoću Arrheniusove jednadžbe [16]:

$$k_k = AT^{\beta} \exp\left(-\frac{E_a}{RT}\right) \tag{5}$$

gdje je k_k globalna brzina kemijske reakcije, A i β su konstante dobivene iz eksperimenta, E_a aktivacijska energija kemijske reakcije, R opća plinska konstanta i T termodinamička temperatura.

Modeli izgaranja nastoje opisati proces izgaranja bez rješavanja transportnih jednadžbi za svaku kemijsku vrstu koja sudjeluje u procesu izgaranja. U ovom radu je korišten ECFM 3Z+ model koji rješava transportne jednadžbe samo za O_2, N_2, CO_2, CO, H_2, H_2O, O, H, N, OH i NO [16]. Dodatno se rješavaju još tri transportne jednadžbe unutar standardnog transportnog modela:

- Gorivo
- Maseni udio goriva
- Maseni udio zaostalih produkata plinova

EKSPERIMENTALNI PODACI

Eksperimentalni podaci dobiveni su od strane Fakulteta strojarstva u Ljubljani, Sveučilišta u Ljubljani u suradnji s prof. Tomažom Katrašnikom. Eksperimentalni dizel motor PSA 1.6 HDi je prikazan na slici 1., dok su njegovi podaci prikazani u tablici 2.

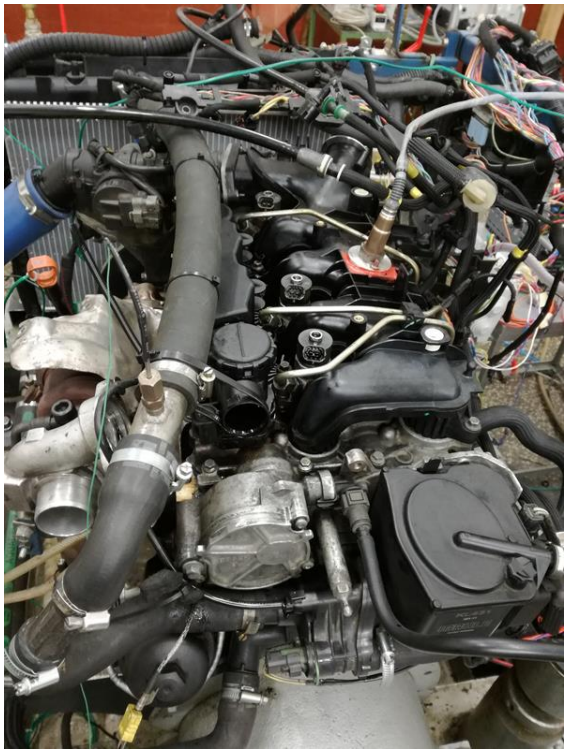

Slika 1. Eksperimentalni PSA 1.6 HDi dizel motor

Tablica 2. Podaci o motoru

Broj cilindara	4 (DOHC)
Promjer x Stapaj, mm	75 x 88,3
Kompresijski omjer	18

Geometrija klipa prikazana na slici 2. izmjerena je pomoću 3D skena na temelju kojeg se izradila računalna mreža. Za modeliranje spreja bili su potrebni podaci o brizgaljci koja je prikazana na slici 3. Podaci o brizgaljci su dani u Tablici 3.

U eksperimentalnom motoru tijekom rada motora klip se hladio uljem, dok se glava motora hladila vodom. Detalji dva promatrana radna stanja eksperimentalnog motora prikazani su u Tablici 4. Za promatrana radna stanja motora mjeren je tlak u cilindru, iz kojeg je izračunata krivulja srednje temperature i krivulja brzine oslobađanja topline.

Slika 2. Klip eksperimentalnog PSA 1.6 HDi dizel motora

Slika 3. Brizgaljka eksperimentalnog PSA 1.6 HDi dizel motora

Tablica 3. Podaci o brizgaljci

Broj otvora na sapnici	6
Promjer otvora sapnice	0.115 mm
Kut spreja	149 °
Promjer igle	4.0 mm

Tablica 4. Eksperimentalni podaci za dva radna stanja motora

Radno stanje		1	2
Gorivo	Norm	EN 590	
Brzina vrtnje	min-1	1499.60	1500.18
Početak i trajanje glavnog ubrizgavanja goriva	CA (°)	714	716
	μs	545	710
Tlak ubrizgavanja	bar	700	840
Početak i trajanje pred ubrizgavanja	CA (°)	695	687
	μs	240	280
Maseni protok goriva	kg/s	0.000623	0.000990
Tlak poslije kompresije	bar	11.702	12.600
Temperatura goriva	°C	17.81	19.11
Temperatura rashladne vode	°C	92.33	94.21
Temperatura ulja	°C	<107.75	107.75

NUMERIČKE POSTAVKE

Mreža za numeričke simulacije generirana je pomoću AVL ESE Diesel programskog paketa. Za dva radna slučaja generirane su dvije mreže s istom topologijom, ali s različitim kompenzacijskim volumenom. Za prvo istraživano radno stanje motora kompenzacijski volumen se nalazio na klipu, dok se u drugom radnom stanju nalazio u prostoru zračnosti između klipa i glave motora kada je klip pozicioniran u gornjoj mrtvoj točci. Ispitan je utjecaj mreže na rezultate simulacije, te je odabrana adekvatna računalna mreža. Zadani rubni uvjeti numeričke simulacije, za oba radna stanja motora, prikazani su u Tablici 5.

Tablica 5. Rubni uvjeti

Temperatura klipa	160 °C
Temperatura glave motora	120 °C
Temperatura stjenke cilindra	120 °C
Os	Simetrija
Segment	Cirkulacija

Na slici 4. prikazana je mreža s rubnim uvjetima za radno stanje 1. Napravljena je mreža samo za šestinu geometrije klipa, jer sapnica ima 6 rupa za ubrizgavanje goriva.

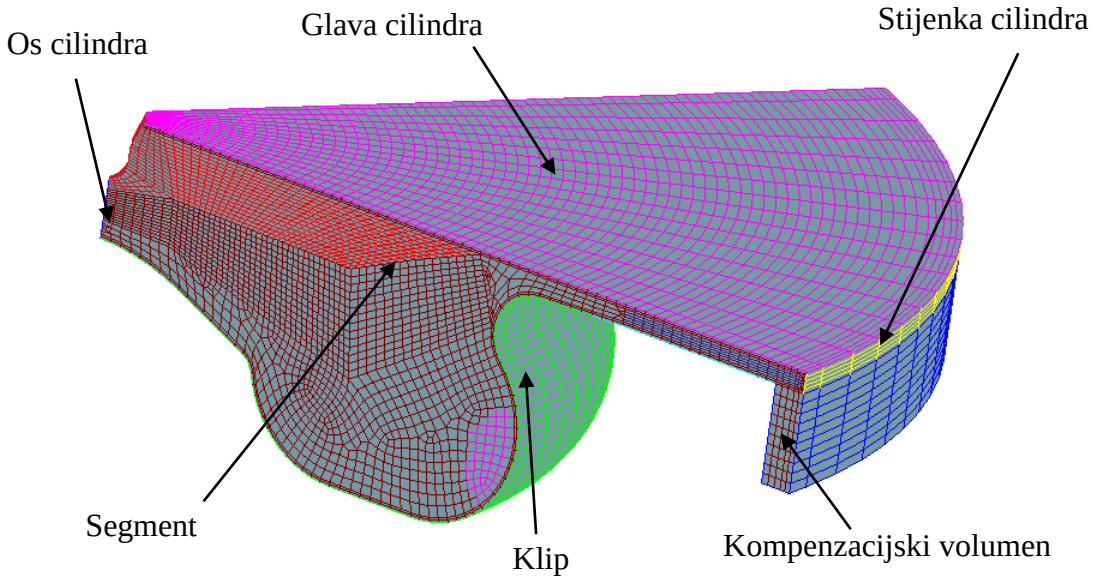

Slika 4. Mreža s definiranim selekcijama za rubne uvjete

Svi podaci o ubrizgavanju goriva nisu poznati, stoga je potrebno bilo donijeti neke pretpostavke. Naime, iz eksperimentalnih ispitivanja poznata je samo ukupna masa goriva ubrizganog u jednom ciklusu rada motora, te trajanje pojedinih ubrizgavanja. Profil ubrizgavanja goriva i masa goriva ubrizgana u pred ubrizgavanju i glavnom ubrizgavanju nisu poznate te su stoga pretpostavljene. Pretpostavljeni profil ubrizgavanja goriva prikazan je na slici 5.

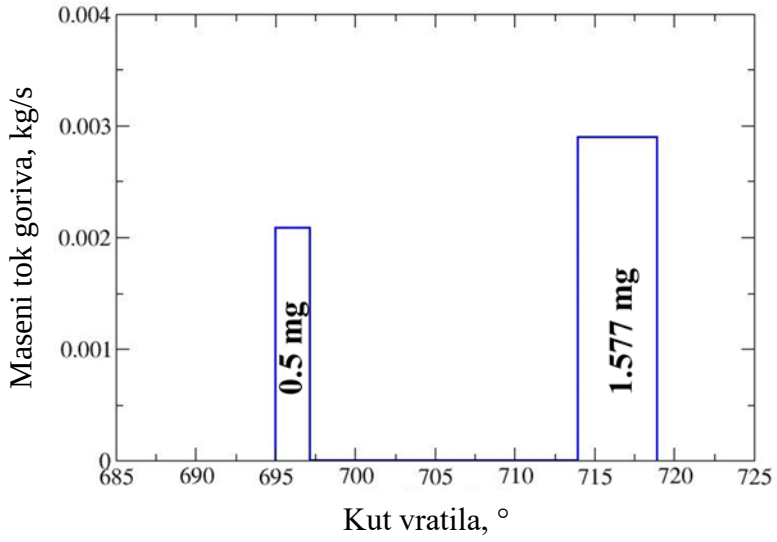

Slika 5. Pretpostavljeni profil ubrizgavanja goriva za radno stanje 1

Pretpostavljeni profil ubrizgavanja za radno stanje 2 ekvivalentan je kao za radno stanje 1, te je prikazan na slici 6. Za simulacije radnog stanja 2 sve numeričke postavke spreja su iste kao i za radno stanje 1. U tablici 6. su prikazane postavke spreja za oba slučaja. U glavnom radu je detaljnije opisan odabir parametara spreja.

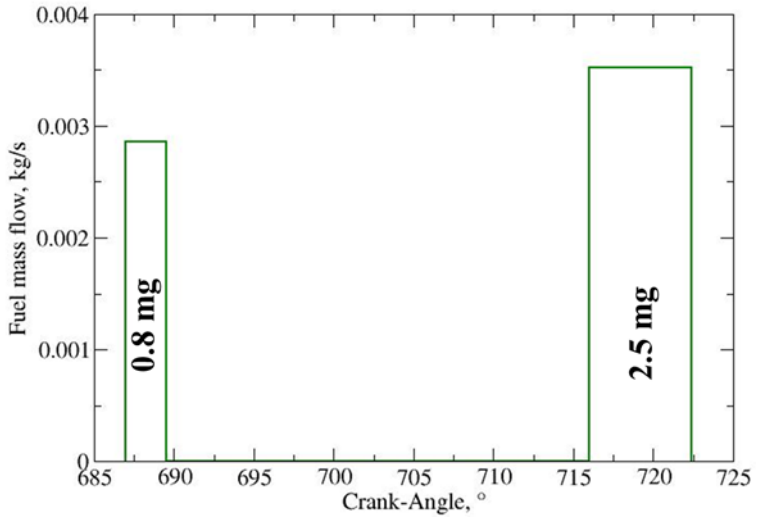

Slika 6. Pretpostavljeni profil ubrizgavanja goriva za radno stanje 2

Tablica 6. Numeričke postavke spreja za oba radna stanja

	Pred ubrizgavanje	Glavno ubrizgavanje
WAWE konstanta C_2	15	15
Pola kuta konusa spreja	10	7

REZULTATI

Svi dobiven rezultati simulacija u radu prikazani su u usporedbi s eksperimentalnim podacima. Punim krivuljama su prikazani rezultati simulacija, a s crnim točkama su prikazani rezultati eksperimentalnog ispitivanja. Jedan od zadataka ovog rada bilo je prikazati usporedbu rezultata modela izgaranja ECFM 3Z+ i kemijskog mehanizma. Za opisivanje procesa izgaranja korišten je kemijski mehanizam za n-heptan C_7H_{16} s 57 kemijskih vrsta i 293 kemijskih jednadžbi. U ECFM 3Z+ modelu izgaranja korišteno je dizel gorivo prema normi EN 590 koje se koristilo i u eksperimentalnom ispitivanju motora. Rezultati po volumenu prosječnog tlaka za ECFM 3Z+ model izgaranja i za kemijski mehanizam prikazani su na slici 7. Rezultati simulacija se

poklapaju za područje kompresije plina u cilindru. Do razlike u rezultatima dolazi tek nakon procesa samozapaljenja isparenog goriva u pred ubrizgavanju. Tijekom procesa izgaranja, tlak kemijskog mehanizma bio je viši od tlaka modela izgaranja, što se najviše može pripisati različitim svojstvima goriva. Model izgaranja i kemijski mehanizam pokazuju rezultate tlaka iznad eksperimentalnih podataka.

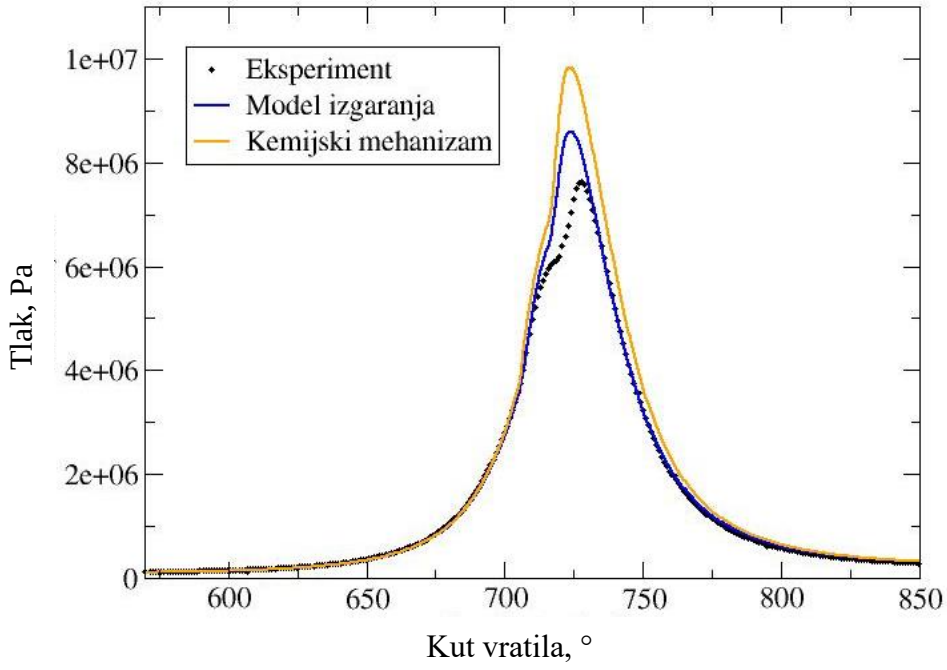

Slika 7. Usporedba rezultata tlak između modela izgaranja i kemijskog mehanizma za radno stanje 1

Rezultati po volumen prosječne temperature u cilindru prikazani su na slici 7. Razlika između modela izgaranja i kemijskog mehanizma vidljiva je također iz rezultata po volumenu prosječne temperature koji su prikazani na slici 8. Rezultati simulacija po volumenu prosječne temperature djelomično su slični s rezultatima na slici 7. Temperature izračunate simulacijama ne poklapa se s rezultatima eksperimenta nakon izgaranja, odnosno tijekom ekspanzije cilindra.

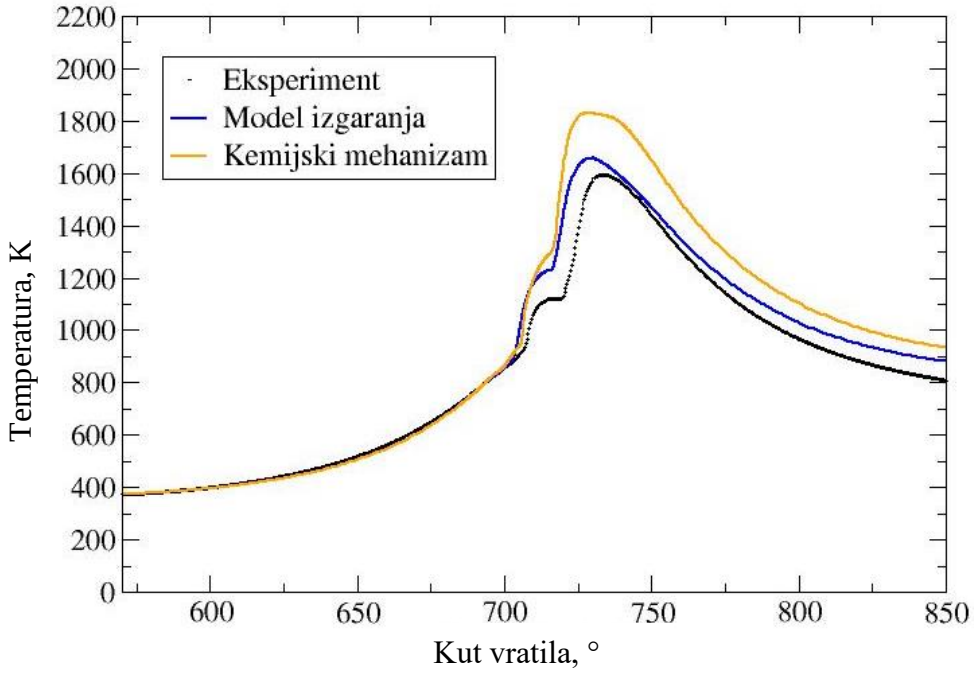

Slika 8. Usporedba rezultata temperature između modela izgaranja i kemijskog mehanizma za radno stanje 1

Rezultati po volumenu prosječnog tlaka u usporedbi s eksperimentalnim podacima prikazani su na slici 9. Rezultati tlaka za radno stanje 2 pokazuju veće odstupanje od eksperimenta u usporedbi s radnim stanjem 1. Tlak izračunat simulacijom prikazuje niže vrijednosti za period kompresije plina u cilindru.

Na slici 10. prikazani su rezultati po volumenu prosječne temperature za radno stanje 2. Rezultati prikazuju značajno bolje poklapanje s vrijednostima eksperimenta za vrijeme ekspanzije cilindra nego rezultati u radnom stanju 1.

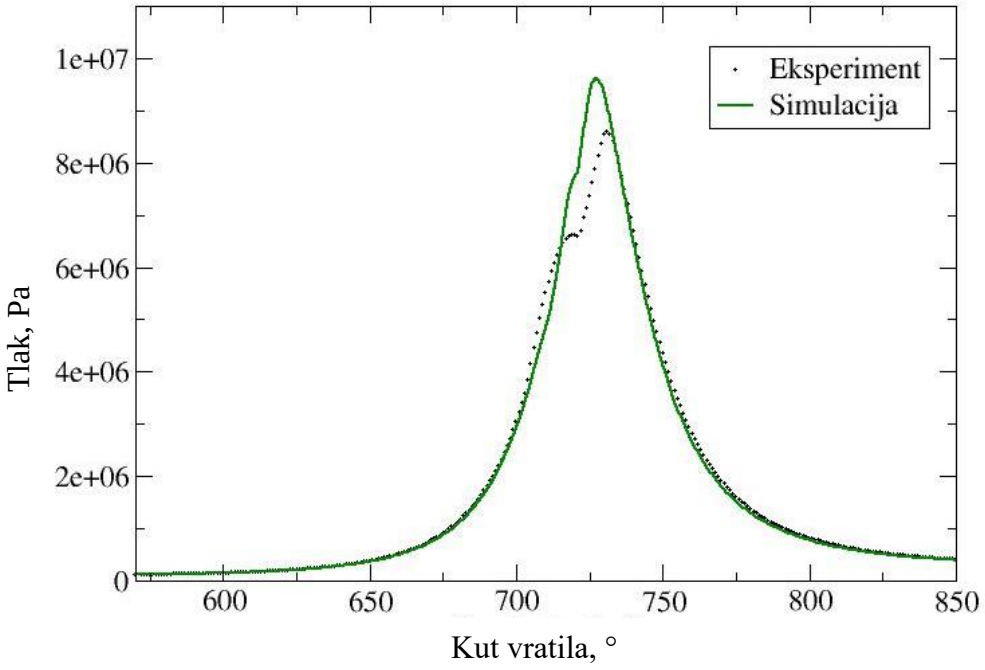

Slika 9. Usporedba po volumenu prosječnog tlaka između rezultata simulacije i eksperimenta

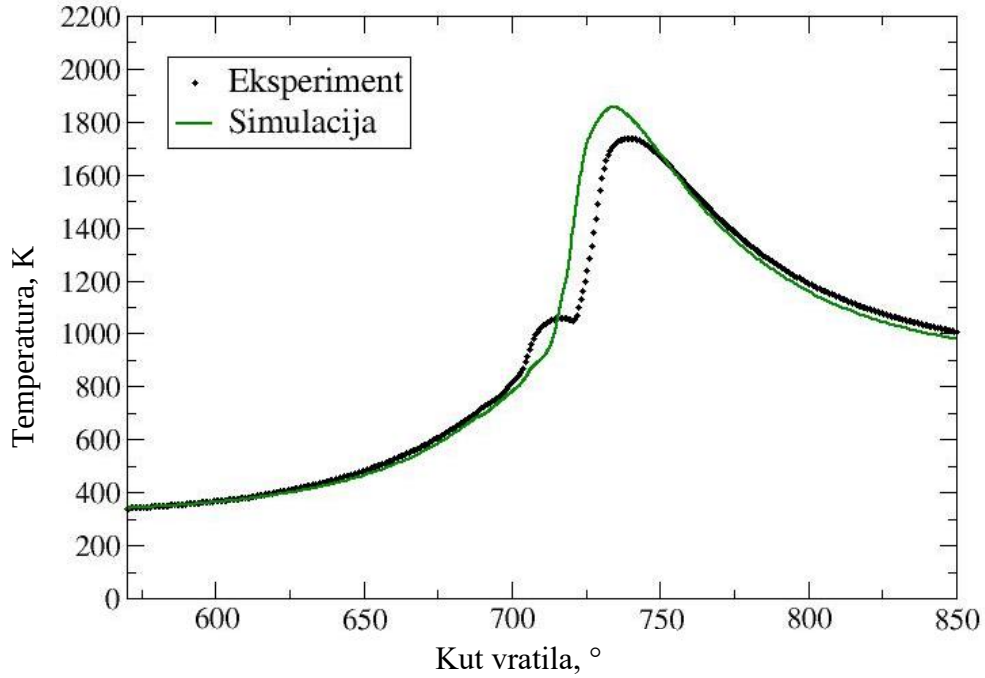

Slika 10. Usporedba po volumenu prosječne temperature između rezultata simulacije i eksperimenta

1. INTRODUCTION

It is known that 93 % of final energy consumption for transport makes oil products, which are making this sector least diversified [1]. Currently, in Europe is the diesel to gasoline ratio around the 2.6 value, as shown in Figure 1. This ratio is still increasing, due to a slight increase in diesel fuel consumption and a fast decrease in gasoline fuel consumption. The reason for that trend in the European countries is a higher energy conversion, higher power output, noise reduction, high durability, and reliability of the Internal Combustion (IC) diesel engines [3].

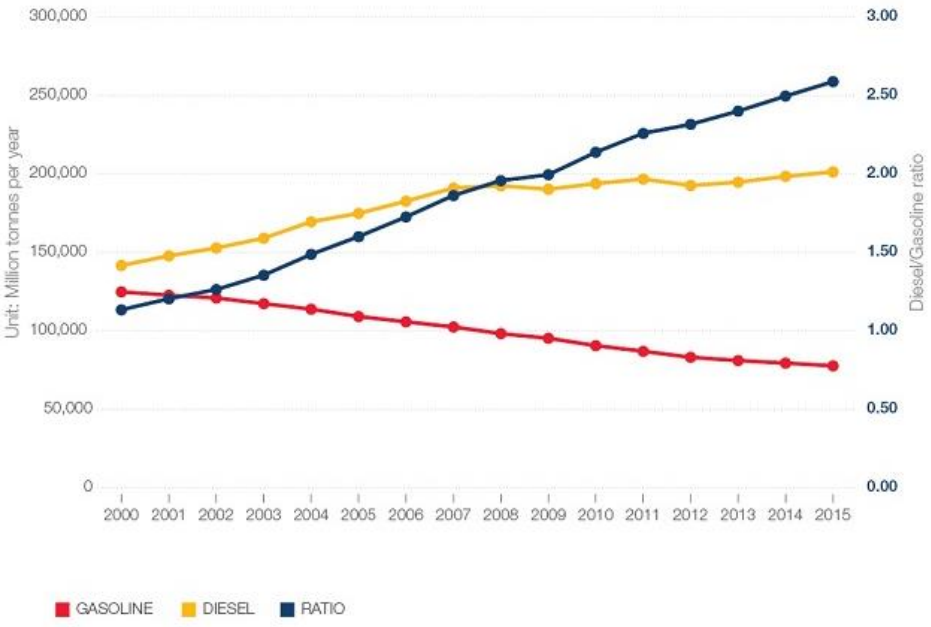

Figure 1 Road fuel demand in the EU [2]

It is known that the spray process has an influence on system efficiency that can be increased by optimising certain mathematical models. The significance of developing spray modelling in diesel engines presents fundamental and initial data for the more accurate emission modelling. The understanding of spray and combustion process, and their improvement can have a significant impact on emission formation. With every new Euro standard, the prescribed diesel engine pollutant emission is lower. Therefore, the development of spray mathematical models can have a significant role in emission reduction.

1.1. Diesel engine

Diesel engines are Compression Ignition (CI) engines, where the rise in temperature and pressure during the compression stroke is sufficient to cause spontaneous fuel ignition. There are two main classes of diesel combustion chamber:

- Diesel engine with Direct Injection (DI) into the main chamber
- Diesel engine with Indirect Injection (ID) into some form of divided chamber

DI diesel engines have less air motion than indirect injection diesel engines. For that reason, in DI engines the high injection pressures (up to 1500 bar and higher) in combination with multiple-hole nozzles are used to achieve better fuel-air mixing process [4]. The purpose of a divided combustion chamber is to speed up the combustion process and to increase the engine output by increasing engine speed.

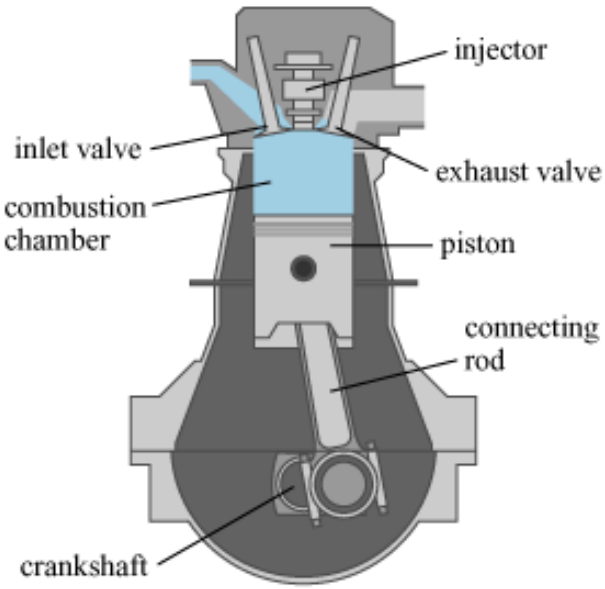

Figure 2 Cut section of direct injection diesel engine [5]

Figure 2 shows DI diesel engine in the cut section with its main parts. The inlet and exhaust valve are used for regulating in-cylinder pressure, and for the exchange of exhaust gases with fresh air (oxygen, that is required for combustion process). The injector is used to introduce the diesel fuel into the combustion chamber, where it burns. The expansion of combustion product gases results in piston movement. The connecting rod transfers the linear piston motion into the rotation movement to the crankshaft, which is then used as the output power.

1.1.2. Ideal Diesel cycle

Ideal Diesel cycle consists of two isentropic (adiabatic), one isobaric and one isochoric process. Figure 3 shows a pressure-volume diagram for the ideal Diesel engine cycle with four distinct processes [7]:

1. From a to b is isentropic compression of the fluid
2. From b to c is constant pressure combustion
3. From c to d is isentropic expansion
4. From d to a is reversible constant volume cooling

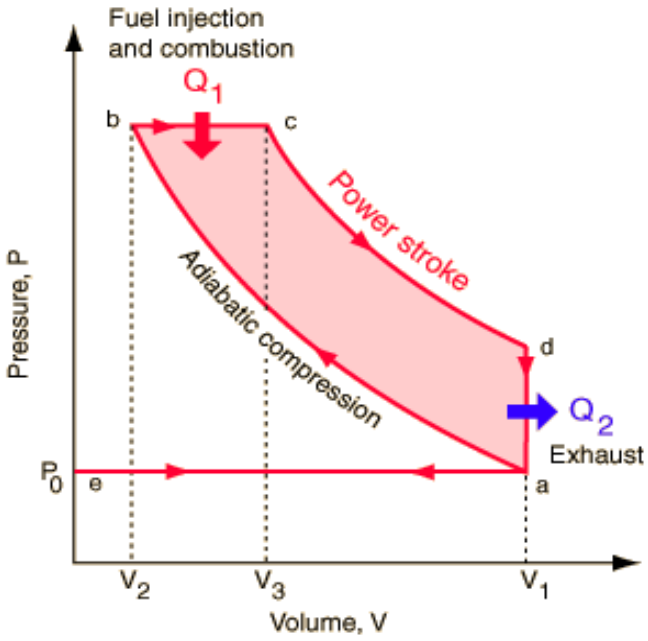

Figure 3 Pressure-volume diagram for the ideal Diesel engine working cycle [8]

The points a and d in Figure 3. are known as Bottom Dead Centre (BDC), and point b is referred to as Top Dead Centre (TDC). The length difference between BDC and TDC of the piston is called piston stroke. The piston stroke distance is also same as the crankshaft diameter (diameter where the connecting rod is linked with crankshaft). At the point a, the inlet and the exhaust valves are closed, the piston is switching movement direction, and the adiabatic compression starts. In the ideal Diesel cycle, adiabatic compression lasts until the point b, at which fuel injection starts. Because temperature at point b is higher than fuel ignition temperature, the combustion starts together with isobaric expansion and the heat is released. At the point c, adiabatic expansion begins, which is also called the power stroke. At the point d, adiabatic

expansion ends. Afterwards, the exhaust valve opens, and the exhaust gases are blown out from the combustion chamber.

1.1.3. Compression ratio

One of the fundamental parameters that describe Diesel engine working cycle is compression ratio. Compression ratio is a value that presents the proportion of the cylinder volumes in the BDC and TDC. In Figure 3 for the ideal Diesel cycle, the compression ratio is expressed as the ratio between the engine working volume V_1 and volume V_2. The efficiency of the engine increases with higher values of compression ratio. However, the maximum pressure reached in the cylinder also increases, i.e. the top value of compression ratio is limited with mechanical properties of cylinder material. It could be stated that the compression ration is always a compromise between high efficiency and low weight and manufacturing costs. The typical compression ratios are in the range from 14 to 17 but may be up to 23 [9] The minimum compression ratio when the combustion occurs in CI engines is about 12. Due to compression ignition, the mass air-fuel ratios used in Diesel engines are in between of 18 and 25 [9].

1.2. Combustion in Diesel engine

Combustion is an exothermic process, where air-fuel mixture through the chemical reactions releases chemically bounded energy. The fuel injection and combustion processes occur when the position of the piston is near the TDC, contrary to exhaust process when piston position is at the BDC. In CI engine, the combustion process occurs due to the high-temperature conditions produced by the compression of the in-cylinder gas mixture. This process is known as diesel fuel auto-ignition process. After fuel injection, the liquid fuel undergoes a series of process in order to assure a proper combustion [10]:

1. Atomization
2. Evaporation
3. Mixing
4. Auto-Ignition

Atomization process is defined as a disintegration of the bulk liquid into a large number of droplets and unstable ligaments caused by the internal and external forces occurring as a result of the interaction between the liquid fuel and ambient gas [11]. The liquid fuel atomization is described with three processes: the internal flow in the nozzle; the breakup of the liquid jet; and

the breakup of the liquid droplets [11]. The atomization process significantly improves the efficiency of the evaporation process, since the surface area for evaporation is increased. Each fuel droplet within the engine cylinder is quickly surrounded by the layer of fuel vapour. The latent heat for phase change of the liquid fuel is absorbed from the surrounding gas mixture. As a result of that, the temperature in spray region is reduced. After evaporation process, the fuel vapour must mix with hot surrounding air to form a combustible mixture. The mixing process is mainly determined by a value of the fuel injected velocity and with a swirl inside the cylinder. The quality of mixing is described with the air-fuel ratio, which is not homogenous inside the cylinder. The mixture is close to stoichiometric air-fuel ratio only at the flame front. After the combustible mixture is made, the air-fuel mixture starts to auto-ignite. Before the combustion, large hydrocarbon molecules are broken into smaller species. At the same time, high-temperature gas is causing oxidation of smaller species. The energy released by the oxidation of large hydrocarbons raises the gas temperature in the spray region. When the ignition starts, the further required heat for evaporation of the last injected droplets will be absorbed from the energy released by the combustion of the first injected droplets. That finally leads to a sustained combustion process.

In CI engine, the flame is non-premixed and turbulent, usually referred as the diffusion flame. Figure 4 shows a fuel injected in ambient air, where reaction zone is fed by oxygen due to air-entrainment. Typically for turbulent non-premixed flames is the diffusion of fuel and air toward the flame zone.

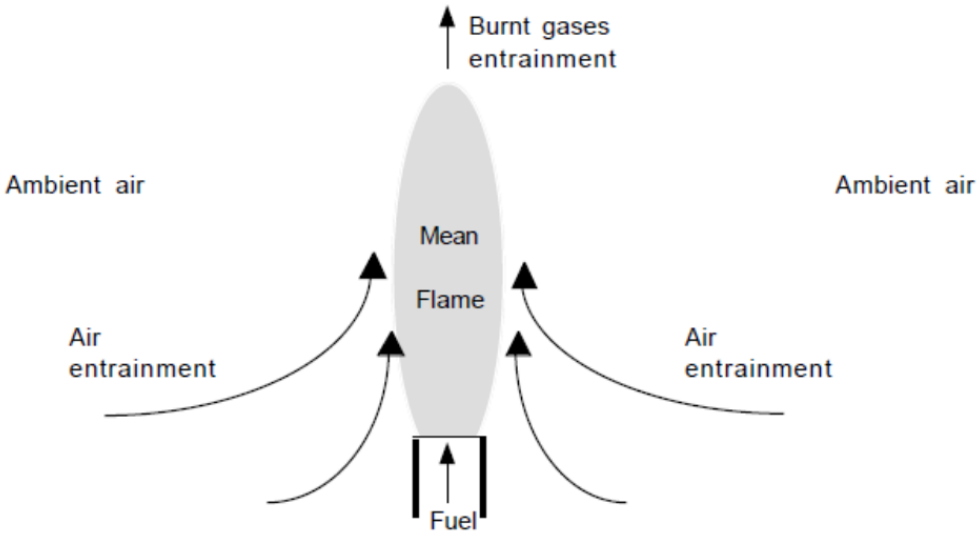

Figure 4 Schematic of turbulent non-premixed flame [12]

1.2.1. Swirl motion

Despite the variety of shapes, all properly designed combustion chambers are claimed to give an equally good performance regarding fuel economy, power and emissions. The geometry of the combustion chamber is less critical than the carefully produced air motion inside the cylinder and selected injection rate [6]. The most significant air motion in direct injection CI engines is swirl, which is defined as the rotation of gases inside the cylinder. The design of the inlet valves and suitably shaped inlet ports are used to produce the swirl motion (value and direction of rotation).

In the CI engine, the swirl is a mean rotational movement of the gas inside the combustion chamber [6]. If the air within the cylinder is motionless, the air and fuel will be less mixed, and less fuel will be in contact with surrounding oxygen molecules. The function of the swirl motion is to distribute the droplets uniformly through the combustion space, i.e. to make a homogeneous mixture with approximately equal air-fuel ratio through the combustion chamber. The function of swirl is also to supply the fresh air to each burning droplet and to sweep the gas products from burning droplets, which otherwise tend to make a barrier for fresh air. The swirl rotation around the axis of the cylinder is shown in Figure 5. Modelling of swirl in CFD simulations is based on three parameters: point of the rotation axis, the direction of the rotation axis and swirl value. The rotation axis of swirl is also the symmetry axis of the cylinder which is shown with a blue line in Figure 5.

Figure 5 Gas swirl motion inside the IC engine cylinder [13]

1.3. Computational Fluid Dynamics

Using Computational Fluid Dynamics in combination with experimental research has become a standard approach in the development of combustion systems. Besides the significant reduction of time and costs in designing modern combustion systems, CFD simulations can be used as a research tool to analyse turbulence, reacting multiphase flows, physical and chemical processes, etc. [14]. The main focus of CFD combustion simulations is to get detailed output data of combustion process, e.g. temperature field, evaporated fuel, flame structure, emission, etc., that will be later used to evaluate the design, possible improvements or development of the observed IC engine combustion chamber. Insights in the fundamental combustion processes will provide the technical background required to solve combustion problems.

Figure 6 shows theoretical CFD combustion model workflow. A mathematical model is the central part of CFD simulation. The equation needed to describe combustion system are based on conversation and transport laws of quantity. A mathematical model of every physical and chemical phenomenon (that was described in chapter 1.2.) is required for the CFD combustion simulation. All input data, as shown in Figure 6, for CFD simulation is implemented in the mathematical model.

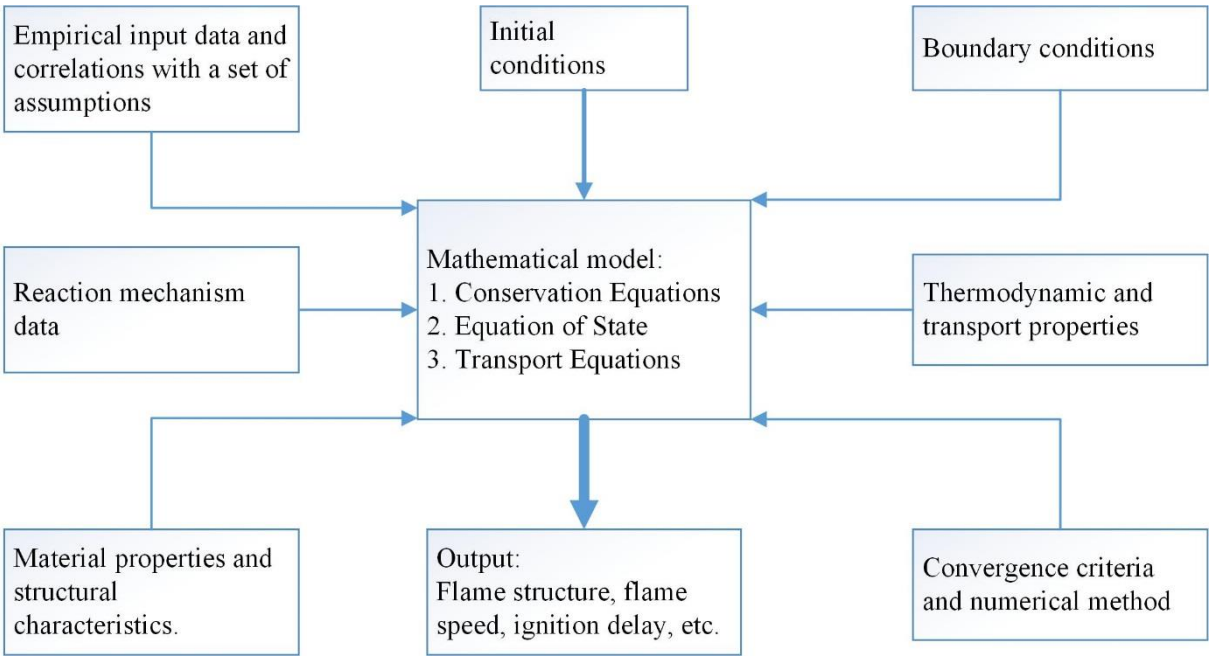

Figure 6 Theoretical workflow of CFD model

The conservation and transport equation for continuum cannot be solved analytically for such a complex process as combustion in Diesel engine. The only option to solve that process is numerical with the discretization of those equations. Finite Volume Method (FVM) is commonly used for discretization in CFD simulations because the FVM is strictly conservative. The FVM makes the transformation of partial differential equations of representing conservation laws over differential volumes into discrete algebraic equations over finite volumes [14].

2. MATHEMATICAL MODEL

The combustion engineers and scientists are often confronted with complex phenomena which depend on interrelated processes of fluid mechanics, heat transfer, mass transfer, chemical kinetics, thermodynamics, turbulence, and spray [15]. For describing each of these processes, mathematical models are needed. The focus of every CFD simulation is solving problems of fluid mechanics by employing the numerical method.

The main assumption of the mathematical model in this work is that gas inside the cylinder is the continuum. On the other hand, the liquid fuel phase is considered as Lagrangians' fluid parcels. For that purpose, the conservation equations in this chapter are based on single gas phase flow. In continuum mechanics, conservation laws are derived in integral form, considering the total physical quantity within the control volume. Conservation laws for fluid flow are written in the integral form, for the reason that the integral form is used for calculations in CFD.

2.1. Conservation laws for a control volume

The conservation equations can be obtained by using the finite volume approach, where the fluid flow is divided into control volumes. The mathematical model in this work is developed for the finite control volume.

The conservation equations are presented for the following dynamic and thermodynamic properties:

1. Mass → Equation of Continuity
2. Momentum → Equation of Motion (Newton's second law)
3. Energy → The first Law of Thermodynamics

2.1.1. Mass conservation equation

The mass of control volume element can only be changed if the inflow through element's boundaries is different from the outflow. The mass within the control volume will decrease if the outflow is higher than the inflow, and in the opposite case, it will increase. Integral form of mass conservation for a fixed spatial control volume element V can be expressed as:

$$\int_S \rho\, u_i\, n_i\, dS = -\frac{\partial}{\partial t}\int_V \rho\, dV \tag{1}$$

The rate of mass flux through element boundary surface *S* is represented as a term on the left-hand side of equation (1), which is equal to the time rate of total mass change in the control volume *V* shown on the right-hand side of equation (1).

2.1.2. Momentum conservation equations

Conservation of momentum is derived from Newton's second law. The sum of the volume and surface forces acting on a fluid control volume element is equal to the time rate of momentum change of the fluid control volume element. Integral form of momentum conservation for a fixed spatial control volume element V can be expressed as:

$$\int_V \frac{\partial}{\partial t}(\rho\, u_j)\, dV + \int_S \rho\, u_j\, u_i\, n_i\, dS = \int_V \rho\, f_j\, dV + \int_S \sigma_{ij}\, n_i\, dS \tag{2}$$

Equation (2) is written in index notation, where the momentum is a vector with three components (j = 1, 2, 3). Each component describes the value of momentum in Cartesian coordinate system and presents one scalar equation. The time rate of momentum change of the control volume element *V* is represented as a first term on the left-hand side of equation (2). The second term on the left-hand side of equation (2) accounts for the sum rate of the flux through element boundary surface *S*. The sum of volume forces acting on the control volume element is represented by the first term on the right-hand side of equation (2), and the second term on the right-hand side is the sum of surface forces acting on the control volume element.

If the fluid is Newtonian, fluid stress tensor σ_{ij} can be written as:

$$\sigma_{ij} = -p\delta_{ij} + \tau_{ij} \tag{3}$$

where p is absolute pressure, δ_{ij} is Kronecker delta, and τ_{ij} is viscous stress. By definition of a Newtonian fluid, the viscous stress τ_{ij} is linearly proportional to the rate of deformation:

$$\tau_{ij} = \mu\left(\frac{\partial u_i}{\partial x_j} + \frac{\partial u_j}{\partial x_i}\right) - \frac{2}{3}\mu\, \delta_{ij}\frac{\partial u_k}{\partial x_k} \tag{4}$$

where μ is the homogeneous fluid viscosity. Taking into account equations (3) and (4) momentum conservation equation can be expressed as:

$$\int_V \frac{\partial}{\partial t}(\rho\, u_j)\, dV + \int_S \rho\, u_j\, u_i\, n_i\, dS = \int_V \rho\, f_j\, dV - \int_S p\, n_i\, dS + \int_V \mu \frac{\partial^2 u_i}{\partial x_i \partial x_i}\, dV \qquad (5)$$

Equation (1) and (5) are together called Navier-Stokes equations.

2.1.3. Energy conservation equation

Energy cannot be destroyed, it can only be converted from one form to another, and the total energy of the system remains constant. The rate of energy change equals the sum of the rate of heat transfer and the power of forces on the fluid particle. The integral form of energy conservation equation can be expressed as:

$$\int_V \frac{\partial}{\partial t}(\rho\, e)\, dV + \int_S \rho\, e\, u_i\, n_i\, dS = \int_V \rho\, f_i\, u_i\, dV + \int_S \sigma_{ij}\, u_i\, n_j\, dS - \int_S q_i\, n_i\, dS + \int_V S_e dV \qquad (6)$$

The first term on the left-hand side of equation (6) represents the rate of total energy change, while the second term on the left-hand represents the total energy transfer across the control volume boundaries. The first term on the right-hand side is the power of volume forces, and the second term is the power of surface forces acting on the control volume boundaries. The both terms are similar as in momentum conservation equation. The third term on the right-hand side is the rate of heat transfer through the control volume boundaries. In the last term on the right-hand side, S_e denotes the volumetric distributed internal heat source due to radiation or chemical reactions. Equation (6) is also the first law of thermodynamics because the first law of thermodynamics is derived from the conservation of energy.

If the fluid is Newtonian, fluid stress tensor σ_{ij} can be written as in equation (3). The heat transfer through the control volume boundaries or heat flux can be written in the form of heat conduction Fourier's law:

$$q_i = -\lambda \frac{\partial T}{\partial x_i} \qquad (7)$$

where λ is thermal conductivity coefficient, and T temperature. Taking into account equation (7) energy conservation equation can be stated as:

$$\int_V \frac{\partial}{\partial t}(\rho\, e)\, dV + \int_S \rho\, e\, u_i\, n_i\, dS = \int_V \rho\, f_i\, u_i\, dV + \int_S \sigma_{ij}\, u_i\, n_j\, dS + \int_S \lambda \frac{\partial T}{\partial x_i} n_i\, dS + \int_V S_e dV \qquad (8)$$

2.1.4. Species mass conservation equation

In the case of the combustion process, the conservation equations for each of the chemical species of interest is required. Opposite to mass conservation equation, the source of chemical species inside the control volume can exist. For example, the source of chemical species from chemical reactions. Integral form of energy conservation equation can be expressed as:

$$\int_V \frac{\partial}{\partial t}(\rho\, y_\mathrm{k})\, dV + \int_S \rho\, y_\mathrm{k}\, u_i\, n_i\, dS = \int_S \rho D_\mathrm{k}\, \frac{\partial y_\mathrm{k}}{\partial x_i} n_i\, dS + \int_V S_\mathrm{k} dV \tag{9}$$

where y_k is the mass fraction of the chemical species k (k is not notation index). The term y_k is defined as the ratio between the mass of chemical species k and total mass.

$$y_\mathrm{k} = \frac{m_\mathrm{k}}{m_{total}} \tag{10}$$

The first term on the right-hand side of the Equation (9) is the diffusion term. The diffusion term is modelled by Fick's law that is an analogue to Fourier's law in equation (7). Furthermore, in the diffusion term, constant D_k is called diffusion coefficient, and it is an analogue to thermal conductivity coefficient in heat and mass transfer analogy.

2.1.5. General transport equation

Fundamental physical conservation laws (mass, momentum, energy, species mass) in their original forms are defined as an equilibrium for a control volume. Conservation laws can be formulated that the rate of change of an extensive property is a consequence of the interaction of the control volume element with another element on its boundaries and interaction of control volume internal source or sinks of the extensive property. The form of general transport equation is same as all previously defined conservation equations and can be expressed as:

$$\int_V \frac{\partial}{\partial t}(\rho\, \varphi)\, dV + \int_S \rho\, \varphi\, u_i\, n_i\, dS = \int_S \Gamma_\varphi\, \frac{\partial \varphi}{\partial x_i} n_i\, dS + \int_V S_\varphi dV \tag{11}$$

Unsteady term | Convection | Diffusion | Source/Sink

where φ is extensive property (scalar or vector).

If the extensive properties φ is changed with physical quantity in Table 1, the required conservation law will be obtained from the general transport equation.

Table 1 Extensive property φ

Conservation law	**Extensive property, φ**
Mass	ρ
Linear Momentum	ρu_i
Energy	ρe
Species Mass	y_k

2.2. Turbulence flow

Usually, the fluid flow in the various engineering systems is turbulent, especially fluid flow in the CI engines. The prediction of turbulent flow is essential for solving engineering problems, and therefore a large group of different mathematical models are developed to calculate turbulence. The common way for describing turbulent fluid flow is dividing the quantity into the mean and fluctuating part. This statistical method for turbulent fluid flow can also be applied to the conservation equations, splitting an extensive quantity into a mean and fluctuating component, as shown in next equation.

$$\varphi = \bar{\varphi} + \varphi' \tag{12}$$

where the mean component is defined as:

$$\bar{\varphi} = \frac{1}{\Delta t} \int_{t}^{t+\Delta t} \varphi(x_i, t) dt \tag{13}$$

By averaging Navier-Stokes equations with taking into account equations (12) and (13) the Reynolds Averaged Navier-Stokes (RANS) equations are obtained. Stochastic quantity and its mean value are shown in Figure 5, where the fluctuating component is shown as the distance between stochastic quality and mean curves.

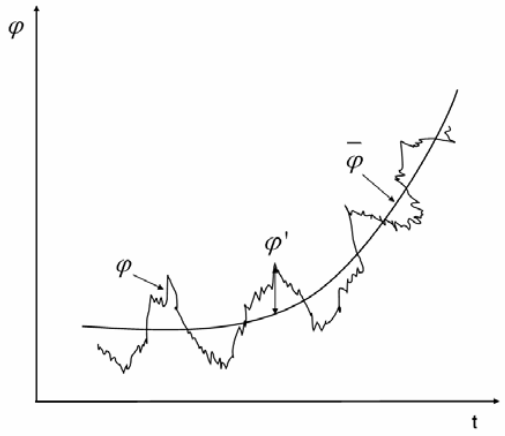

Figure 7 Turbulent fluctuation of fluid flow physical quantity [11]

After application of the Reynolds averaging method, the averaged continuity and momentum equations can be expressed as:

$$\int_S \rho\, \bar{u}_i\, n_i\, dS = 0 \tag{14}$$

$$\int_V \frac{\partial}{\partial t}\left(\rho\, \bar{u}_j\right) dV + \int_S \rho\, \bar{u}_j\, \bar{u}_i\, n_i\, dS = \int_V \rho\, f_j\, dV - \int_S \bar{p}\, n_i\, dS + \int_V \left[\mu\left(\frac{\partial \bar{u}_i}{\partial x_j} + \frac{\partial \bar{u}_j}{\partial x_i}\right) - \overline{\rho u'_i u'_j}\right] dV \tag{15}$$

The time-averaged equations (14) and (15) are called RANS equations. By averaging Navier-Stokes equations, additional term is $\overline{\rho u'_i u'_j}$ obtained, which is called Reynolds stress tensor. Due to recursive characteristic of Reynolds stress tensor, additional correlation between velocity and pressure is needed to solve RANS equations. For that correlation, turbulence models are applied. These models are based on the Navier–Stokes equations up to a certain point, but then they introduce closure hypotheses that depend on requiring empirical input.

2.2.1. Turbulence modelling

Since the flow is turbulent in nearly all engineering applications, the need to resolve engineering problems has led to solutions called turbulence models. They are based on the Boussinesq assumption, which assumes that the Reynolds stress tensor can be modelled in a similar way as the viscous stress tensor. In this work, the k-zeta-f turbulence model was used in all CFD

simulations. The k-zeta-f model is suitable turbulence model that is commonly used in IC Diesel engine combustion simulations [16]. One advantage of the k-zeta-f model is its robustness for modelling strong swirling flows that are characteristic for IC engines.

The k-zeta-f model

This model was developed by Hanjalić, Popovac and Hadžiabdić [17]. The aim of the model is to improve numerical stability of the original $\overline{v^2} - f$ model by solving a transport equation for the velocity scale ratio $\zeta = \frac{\overline{v^2}}{k}$ instead of velocity scale. The turbulent viscosity is obtained from:

$$\mu_t = C_\mu \zeta \rho \frac{k^2}{\varepsilon} \tag{16}$$

where C_μ is model constant, k is turbulent kinetic energy and ε is rate of turbulent energy dissipation, k is defined as:

$$k = \frac{1}{2}\overline{u'_\iota u'_\iota} \tag{17}$$

Moreover, the rest of variables can be obtained from the following set of equations:

$$\rho \frac{Dk}{Dt} = \rho(P_k - \varepsilon) + \frac{\partial}{\partial x_j}\left[\left(\mu + \frac{\mu_t}{\sigma_k}\right)\frac{\partial k}{\partial x_j}\right] \tag{18}$$

$$\rho \frac{D\varepsilon}{Dt} = \rho \frac{(C^*_{e1} P_k - C_{e2}\varepsilon)}{T} + \frac{\partial}{\partial x_j}\left[\left(\mu + \frac{\mu_t}{\sigma_\varepsilon}\right)\frac{\partial \varepsilon}{\partial x_j}\right] \tag{19}$$

$$\rho \frac{D\zeta}{Dt} = \rho f - \rho \frac{\zeta}{k} P_k + \frac{\partial}{\partial x_j}\left[\left(\mu + \frac{\mu_t}{\sigma_\zeta}\right)\frac{\partial \zeta}{\partial x_j}\right] \tag{20}$$

where f can be calculated:

$$f - L^2 \frac{\partial^2 f}{\partial x_j \partial x_j} = \left(C_1 + C_2 \frac{P_k}{\zeta}\right)\frac{\left(\frac{2}{3} - \zeta\right)}{\mathrm{T}} \tag{21}$$

Turbulent time scale T and length scale L are given by:

$$\mathrm{T} = \max\left(\min\left(\frac{k}{\varepsilon}, \frac{a}{\sqrt{6}C_\mu |S| \zeta}\right), C_T \left(\frac{\upsilon}{\varepsilon}\right)^{0.5}\right) \tag{22}$$

$$L = C_L \max\left(\min\left(\frac{k^{1.5}}{\varepsilon}, \frac{k^{0.5}}{\sqrt{6}C_\mu |S| \zeta}\right), C_\eta \left(\frac{\upsilon^3}{\varepsilon}\right)^{0.25}\right) \tag{23}$$

An additional modification to the equation is that the constant $C_{\varepsilon 1}$ close to the wall can be calculated:

$$C^*_{\varepsilon 1} = C_{\varepsilon 1}\left(1 + 0.045\sqrt{\frac{1}{\zeta}}\right) \tag{24}$$

The empirical constants in this model are not universal and must be adjusted to a particular problem. In Table 2, the following set of default values used in the CFD solver FIRE® is shown.

Table 2 The default values of the k-ζ-f turbulence model constants in FIRE®

C_μ	$C_{\varepsilon 1}$	$C_{\varepsilon 2}$	C_1	C_2	σ_k	σ_ε	σ_ζ	C_L	C_η	C_τ
0.22	1.4(1+0.012/ζ)	1.9	0.4	0.65	1	1.3	1.2	0.36	85	6

2.3. Spray modeling

Spray influence the mixing, ignition, combustion and emission processes occurring within the IC engine. For this reason, CFD IC engine simulations highly depend on the quality of spray model. Spray model can consist of several sub-models [18]:

- Primary breakup model, atomization of the liquid jet
- Secondary breakup model, the breakup of the formed liquid drops
- Deformation of the droplets, momentum exchange between the liquid and gas phases
- Collision model, a collision between liquid drops and its possible outcomes
- Wall–film model, the interaction between sprays and walls
- Evaporation model, evaporation of the liquid fuel

The commonly used method for spray calculation is Discrete Droplet Method (DDM) or the Euler Lagrangian spray method [19]. This method tracks the motion of the liquid fuel droplets in the Lagrangian coordinate system. It is practically impossible to solve differential equations for the trajectory, mass transfer, linear momentum and energy transfer of every single spray droplet. Therefore, spray droplets are approximated with groups of droplets that share identical properties. Those groups are called parcels. Every parcel is represented with only one droplet of a certain size for which the differential equations are calculated. The gas phase is calculated with the Eulerian conservation equation. The Lagrangian approach for fuel parcels and Eulerian approach for the gas phase are coupled. The trajectories define the position of parcels in the computational mesh filled with the gas phase. The interaction between the parcel and gas phase can be modelled as a source in conservation equation for the control volume in which the parcel is located. The motion of parcel is described as Newton's second law of motion. The force that has the highest impact on spray forming is the drag force that is generated due to relative velocities.

Deceleration of the parcel is expressed as:

$$m_{\mathrm{p}} \frac{du_{\mathrm{p}i}}{dt} = F_{\mathrm{d}i} \tag{25}$$

where m_p is a mass of the parcel and F_di is drag force. The trajectory of parcel $x_{\mathrm{p}i}$ is calculated by integrating parcel velocity:

$$x_{\mathrm{p}i}(t) = \int_{t}^{t+\Delta t} u_{\mathrm{p}i}\, dt \tag{26}$$

The main disadvantage of this approach is that the computational effort rises with increasing parcel number. Therefore, such approach is usually used to model the sufficiently diluted spray where the volume fraction of the dispersed phase is lower [11].

2.3.1. Spray sub-models

Mathematical models are required to describe the relevant physical phenomena occurring during the injection of Diesel fuel into the pressurised combustion chamber [20]:

- Break-up model → WAVE
- Evaporation model → Dukowicz
- Turbulence dispersion model
- Drag law model → Schiller-Naumann
- Wall interaction model → Walljet1
- Collision model or Particle interaction model

In this chapter, the description of sub-models used in CFD simulation is provided.

WAVE breakup model

The growth of an initial perturbation on a liquid surface of a droplet is linked to its wavelength and other physical and dynamic parameters of the injected fuel and the domain fluid [21, 22]. There are two break-up regimes:

- Rayleigh, for low velocities
- Kelvin–Helmholtz, for high velocities

The Rayleigh regime is not characteristic for high-pressure injection systems, and therefore it will be neglected. In WAVE model all droplets are assumed spherical, and the size of the

product droplets is proportional to the wavelength of the liquid surface wave. The product droplet radius, r_{stable} can be expressed as:

$$r_{stable} = \lambda_w C_1 \tag{27}$$

where C_1 is the WAVE model constants, and λ_w is the wavelength of the fastest growing wave on the parcel surface. The recommended value of C_1 is 0.61. The radius reduction ratio of the parent drops is defined as:

$$\frac{dr}{dt} = -\frac{(r - r_{stable})}{\tau_a} \tag{28}$$

where τ_a is breakup time of the model. The breakup time is calculated as:

$$\tau_a = \frac{3.726 r\, C_2}{\lambda_w\, \Omega} \tag{29}$$

where C_2 is the second WAVE constant, which corrects the breakup time. The constant C_2 varies from one injector to another, so it is used to calibrate the specific injector. Wave growth rate Ω and wavelength λ_w depend on the local flow properties and are calculated as:

$$\Omega = \left(\frac{\rho_d r^3}{\sigma}\right)^{-0.5} \frac{0.34 + 0.38 We^{1.5}}{(1+Oh)(1+1.4 Ta^{0.6})} \tag{30}$$

$$\lambda_w = 9.02\, r \frac{(1+0.45 Oh^{0.5})(1+0.4 Ta^{0.7})}{(1+0.87 We^{1.67})^{0.6}} \tag{31}$$

where Weber number (*We*) and Ohnesorge number (*Oh*) are defined as:

$$We = \frac{2 r \rho u^2}{\sigma} \tag{32}$$

$$Oh = \frac{\mu}{\sqrt{2 r \rho \sigma}} = \frac{\sqrt{We}}{Re} \tag{33}$$

where μ is the liquid viscosity, σ is the surface tension, r is the radius of the droplet (e.g. r_{stable}), ρ is the liquid density, and Taylor number (Ta) is $WeRe^{-1}$ (where Weber number is calculated with a geometric mean density between liquid and gas).

Dukowicz evaporation model

The heat and mass transfer processes in Dukowicz evaporation model are based on following assumptions [23]:

- Spherical droplets
- Quasi-steady gas-film around the droplet
- Uniform droplet temperature along the drop diameter
- Uniform physical properties of the surrounding fluid
- Liquid vapour thermal equilibrium on the droplet surface
- Non-condensable surrounding gas

The correlation for the flux of evaporated fuel can be written as:

$$\dot{m}_{fv} = \frac{q}{Le} \frac{Y_s - Y_\infty}{(1-Y_s)[h_\infty - h_s - (h_s - h_\infty)(Y_\infty - Y_s)]} \tag{34}$$

where all physical quantities:

- with index s are referred to value at the droplet surface
- with index ∞ are referred to value at a long distance from the droplet surface

The Lewis number, Le is unity in the most of the cases (Le = 1), but can also be calibrated with evaporation constants E_1 and E_2. E_1 is called heat transfer parameter, and E_2 is called mass transfer parameter it is a simple multiplicative factor acting on transfer coefficient. Lewis number can be written as:

$$Le = \frac{\mathrm{E1}}{\mathrm{E2}} \frac{\alpha}{D c_p} \tag{35}$$

The Nusselt number, Nu can be obtained from the correlation proposed by Ranz and Marshall [21]:

$$Nu = 2 + 0.6 Re^{0.5} Pr^{0.33} \tag{36}$$

The procedure of the used evaporation model is to solve equation (36) from which the required q can be obtained (from Nu number), and then to solve equation (34.).

Turbulence dispersion

The interaction between fuel droplets and individual turbulent eddies deflects the droplet due to the velocity of the turbulent eddy and the droplet inertia. To solve these additional turbulence effects on the spray droplets, the turbulent dispersion model is employed. The interaction time

of a droplet with the individual eddies is estimated from two criteria, the turbulent eddy life time and the time required for a droplet to cross the eddy. The turbulence correlation time t_{turb} is the minimum of the eddy breakup time and the time for the droplet to pass through the observed eddy, and is given by:

$$t_{turb} = \min\left(\frac{k}{\varepsilon}, 0.16432\frac{k^{1.5}}{\varepsilon|u_g+u'-u_d|}\right) \tag{37}$$

where fluctuation velocity, *u'* is randomly generated from the Gaussian function. If the case has the computational time step larger than the turbulence correlation time t_{turb} the spray integration time step will be reduced to t_{turb}.

Drag law model

The drag force F_{di} in equation (25) is calculated using formulation from Schiller and Naumann.

$$F_{di} = 0.5\pi\, r^2 \rho C_D {u_i}^2 \tag{38}$$

$$C_D = \begin{cases} \frac{24}{ReC_p}(1 + 0.15Re^{0.687}) & Re < 10^3 \\ \frac{0.44}{C_p} & Re \geq 10^3 \end{cases} \tag{39}$$

where r is the droplet radius, ρ density of gas, C_D is the drag coefficient which generally is a function of droplet Reynolds number and C_p is Cunningham correction factor which depends on free path length in the gas phase.

Wall interaction model

The behaviour of a droplet colliding with wall selection depends on several parameters like droplet velocity, diameter, droplet properties, wall surface roughness and wall temperature [20]. In the used wall interaction model, there are two high-velocity regimes, the spread and splash regime. In the spread regime, the complete liquid spreads along the wall with hardly any mass reflection. In the splash regime, a part of the liquid remains near the surface, and the rest of it is reflected and broken up into droplets. Wall interaction model Walljet1 is used in this work. In such model, the vapour layer is formed around the droplets, which promotes their reflection in interaction with the wall. This model does not take into account the liquid wall film physics [23]. The diameter of the droplet after interaction with the wall in both regimes is calculated as a function of Weber number. The droplet reflection angle can vary within $0 < \beta < 5°$ [23].

2.4. Combustion modelling

Combustion modelling can be performed in different ways such as:

- Chemical mechanism
- Combustion model

Chemical mechanism is described with elementary chemical reactions of chemical species.
For each fuel, the chemical mechanism has to be developed with adequate chemical reactions and chemical species which participate in reactions.
In equation (9) volume source S_k can be calculated according to semi-empirical Arrhenius law [16]:

$$k_k = AT^{\beta} \exp\left(-\frac{E_a}{RT}\right) \tag{40}$$

where k_k is the global reaction rate coefficient of a chemical reaction, A and β are coefficient determined from experimental data, and they are unique for every reaction. E_a is reaction activation energy, and it is also determined from experimental research. The chemical species can originate in chemical reactions as products, but they also can be reactants. If the chemical species is a reactant in a chemical reaction, it will be modelled as a sink in its transport equation. The volume source S_k for a chemical species is expressed as a difference between the all forward and backwards reactions, considering the concentration of chemical species in these reactions:

$$S_k = \frac{dc_k}{dt} \cdot M_k = \sum_1^m k_{m,f} \cdot c_m \cdot c_{oxy} - \sum_1^n k_{n,b} \cdot c_n \cdot c_{red} \tag{41}$$

where index *m* is a total number of the forward reactions in which chemical species is a product, and index *n* means the total number of the backwards reactions in which chemical specie is a reactant.
Furthermore, such a complex mechanism could require significant computational power in the simulation of practical combustion systems. The success of turbulence models in solving engineering problems has encouraged similar approaches for turbulent combustion, which consequently led to the formulation of turbulent combustion models. In this work the Coherent Flame Model is used, in which the chemical time scales are much smaller in comparison to the turbulent ones.

Coherent Flame Model

ECFM 3Z+ model is one of coherent flame models suitable for the combustion in Diesel engines. The coherent flame model has a decoupled treatment of chemistry and turbulence, so it makes an attractive solution for combustion modelling.

The ECFM 3Z+ solves transport equations of 11 chemical species: O_2, N_2, CO_2, CO, H_2, H_2O, O, H, N, OH and NO in three mixing zones [16]. The transport equation for each species is calculated as:

$$\frac{\partial \bar{\rho} y_{\mathrm{k}}}{\partial t} + \frac{\partial \bar{\rho} u_i y_{\mathrm{k}}}{\partial x_i} - \frac{\partial}{\partial x_i}\left(\left(\frac{\mu}{Sc} + \frac{\mu_t}{Sc_t}\right)\frac{\partial y_{\mathrm{k}}}{\partial x_i}\right) = \bar{\dot{\omega}}_x \tag{42}$$

where $\bar{\dot{\omega}}_x$ is combustion source term, y_{k} is mass fraction of chemical species k, and $\bar{\rho}$ is mean gas density.

An additional transport equation is used to compute mass fraction of unburned fuel $\tilde{y}_{Fu}^{u}$:

$$\frac{\partial \bar{\rho} y_{Fu}^{u}}{\partial t} + \frac{\partial \bar{\rho} u_i y_{Fu}^{u}}{\partial x_i} - \frac{\partial}{\partial x_i}\left(\left(\frac{\mu}{Sc} + \frac{\mu_t}{Sc_t}\right)\frac{\partial y_{Fu}^{u}}{\partial x_i}\right) = \bar{\rho}\tilde{\dot{S}}_{Fu}^{u} + \bar{\dot{\omega}}_{Fu}^{u} \tag{43}$$

where $\tilde{\dot{S}}_{Fu}^{u}$ is the source term quantifying the fuel evaporation in fresh gases and $\bar{\dot{\omega}}_{Fu}^{u}$ is a source term taking auto-ignition, premixed flame and mixing between mixed unburned and mixed burnt areas into account.

2.5. Species transport

Species transport is divided into two approaches:

- General Species Transport Model
- Standard Species Transport Model

For each chemical species *k*, transport equation is calculated. Sometimes to reduce the calculating time, transport equation for one selected specie is not calculated. Its mass fraction is obtained from stoichiometric equations. The multi-component diffusion between chemical species is available in this model.

The Standard Species Transport is simplified in comparison with the General Species Transport Model. The main task of Standard Species Transport Model is to reduce the number of equations to be solved and to use dimensionless quantities for describing chemical reactions.

Standard Species Transport model consists of three transport equation (11) for:

- Fuel, y_{fu}
- Fuel mixture fraction, f
- Residual gas mass fraction, g

Mass fraction of fuel, y_{fu} is defined as:

$$y_{fu} = \frac{m_{fu,u}}{m_{total}} \tag{44}$$

where $m_{fu,u}$ is unburnt fuel in every cell, and m_{total} is total mixture mass inside the cell. Fuel mixture fraction, f is defined as:

$$f = \frac{m_{fu,u} + m_{fu,b}}{m_{total}} \tag{45}$$

where $m_{fu,b}$ is burnt fuel. Residual gas mass fraction, g is defined as:

$$g = \frac{m_{rg}}{m_{rg} + m_{air}} \tag{46}$$

where m_{rg} is a mass of residual gases. Three transport equation can be expressed as:

$$\int_V \frac{\partial}{\partial t}(\rho\, y_{fu})\, dV + \int_S \rho\, y_{fu}\, u_i\, n_i\, dS = \int_S \Gamma_f\, \frac{\partial y_{fu}}{\partial x_i} n_i\, dS + \int_V S_{fu} dV \tag{47}$$

$$\int_V \frac{\partial}{\partial t}(\rho\, f)\, dV + \int_S \rho\, f\, u_i\, n_i\, dS = \int_S \Gamma_f\, \frac{\partial f}{\partial x_i} n_i\, dS \tag{48}$$

$$\int_V \frac{\partial}{\partial t}(\rho\, g)\, dV + \int_S \rho\, g\, u_i\, n_i\, dS = \int_S \Gamma_g\, \frac{\partial g}{\partial x_i} n_i\, dS \tag{49}$$

This system contains five chemical species: fuel, O_2, CO_2, H_2O, and N_2. But only for fuel is the transport equation calculated (47). The mass fraction of other species is calculated from stoichiometric equations for complete combustion. The less number of equations to be solved for Standard Species Transport model than for General Species Transport model decreases calculation time. Therefore, the Standard Species Transport model represents a suitable tool for engineering applications.

3. EXPERIMENTAL DATA

The experimental data were provided by the Faculty of Mechanical Engineering, the University of Ljubljana in Slovenia and carried out under the direction of professor Tomaž Katrašnik. A four-cylinder PSA Diesel 1.6 HDi engine was examined. In Figure 8 the PSA 1.6 HDi Diesel engine scheme is shown, whilst in Figure 9 experimental engine on which measurements are carried out is shown.

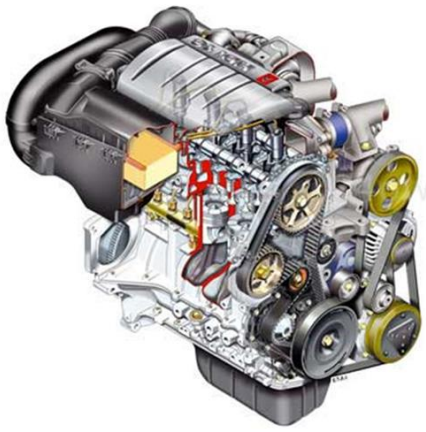

Figure 8 Schematic of PSA 1.6 HDi Diesel engine

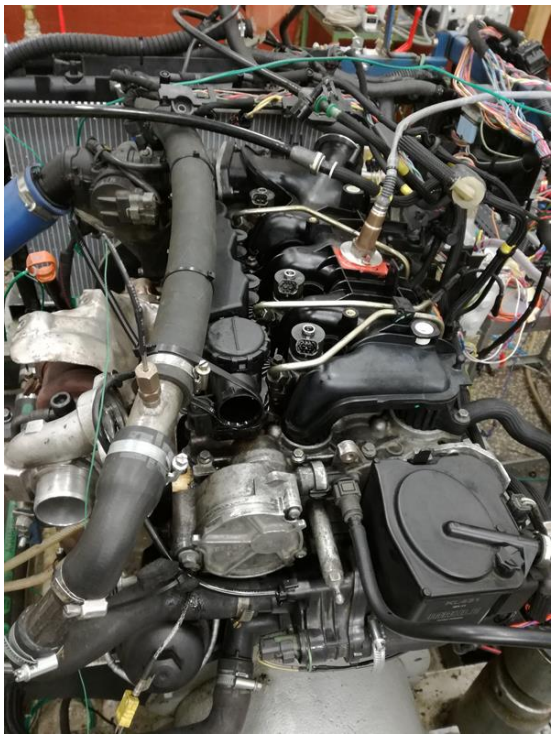

Figure 9 Experimental Diesel engine

Table 3. shows the main specifications of the observed experimental engine. The pressure measurement during the engine working cycle was carried out with a piezoelectric sensor, shown in Figure 10. The experimental data is provided for the engine working cycle from 570° CA (Crank-Angle degrees) to 850° CA. The pressure measured inside the engine cylinder, for two different operating conditions, are presented in Figure 11. Two fuel injections, Pilot Injection (PI) and Main Injection (MI), are present in each engine injection cycle. Therefore, two distinguished auto-ignition processes were recorded in pressure rise, as shown in Figure 11. At approximately 695° CA (depending on the observed case) the PI injection starts. After the fuel injected in PI injection is combusted, the MI injection occurs. The MI injection starts approximately at 715° CA, and it has a higher influence on the pressure increase than combustion of vapour generated from the PI fuel. The influence of fuel multi-injection is also visible in temperature and rate of heat release curves, as shown in Figure 12.

Table 3 Specifications of PSA 1.6 HDi Diesel Engine

Number of cylinders	4
Bore x stroke (mm)	75 x 88,3
Fuel	Diesel EN590
Compression ratio	18

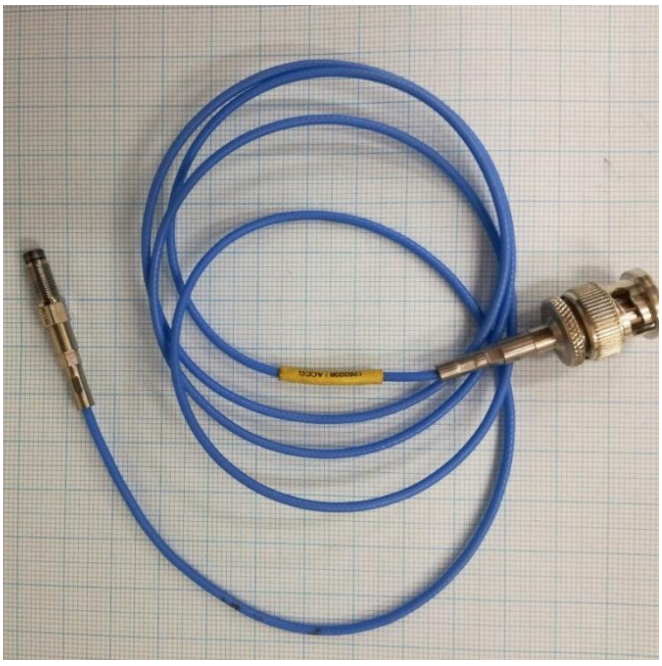

Figure 10 Piezoelectric sensor

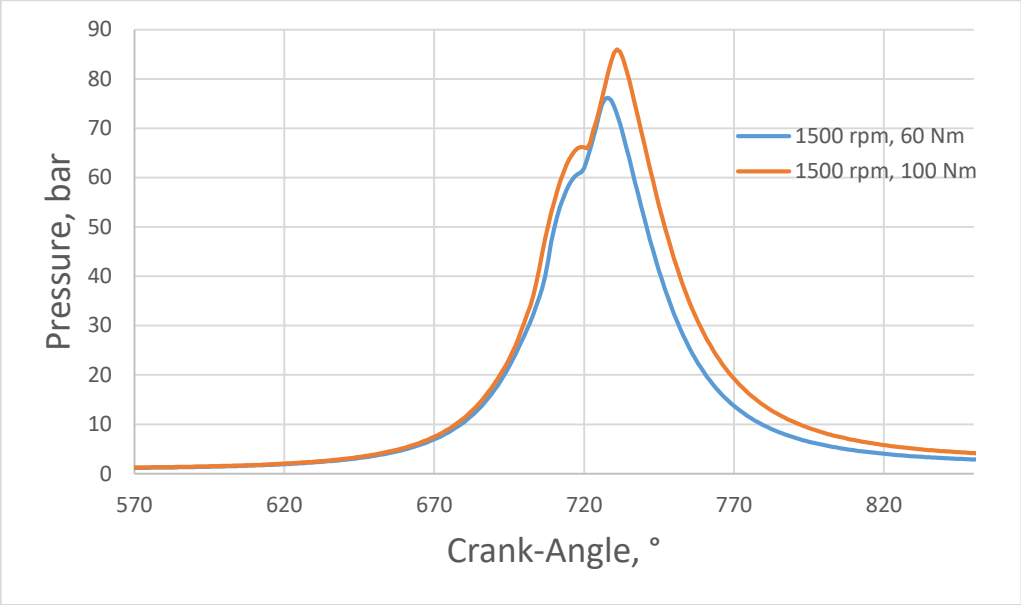

Figure 11 Experimental data of in-cylinder mean pressure

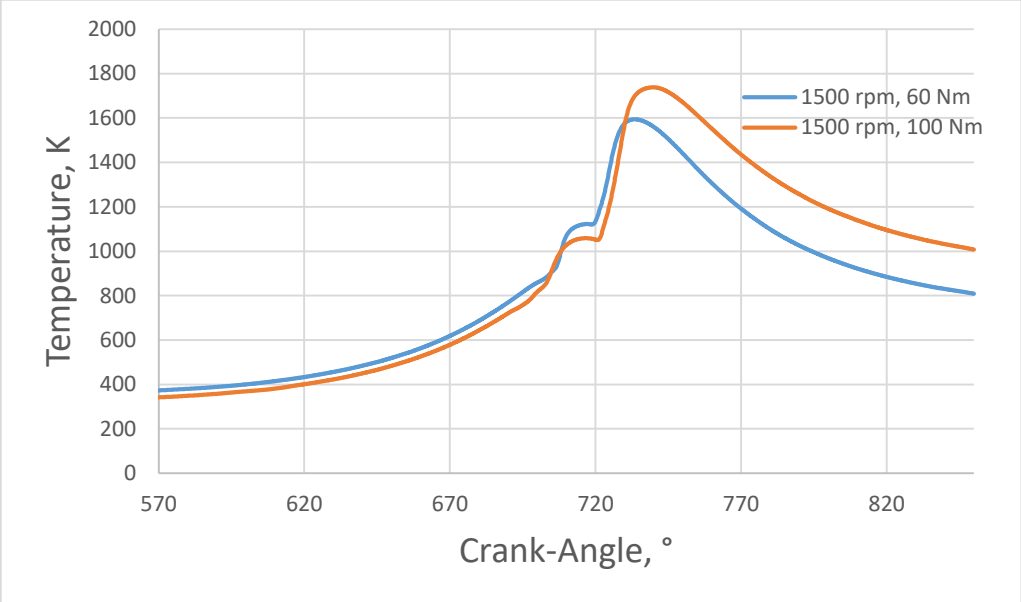

Figure 12 Experimental data of in-cylinder mean temperature

The rate of heat release is a parameter for the evaluation of energy released by fuel combustion. It was calculated from experimental mean pressure data, and it is shown in Figure 13. The area under the curves in Figure 13 is the amount of energy that is released by fuel combustion. The combustion of main injected fuel starts after 720°CA. The amount of energy released in the

combustion of main injected fuel is greater comparing to the energy generated in PI due to a larger amount of injected fuel.

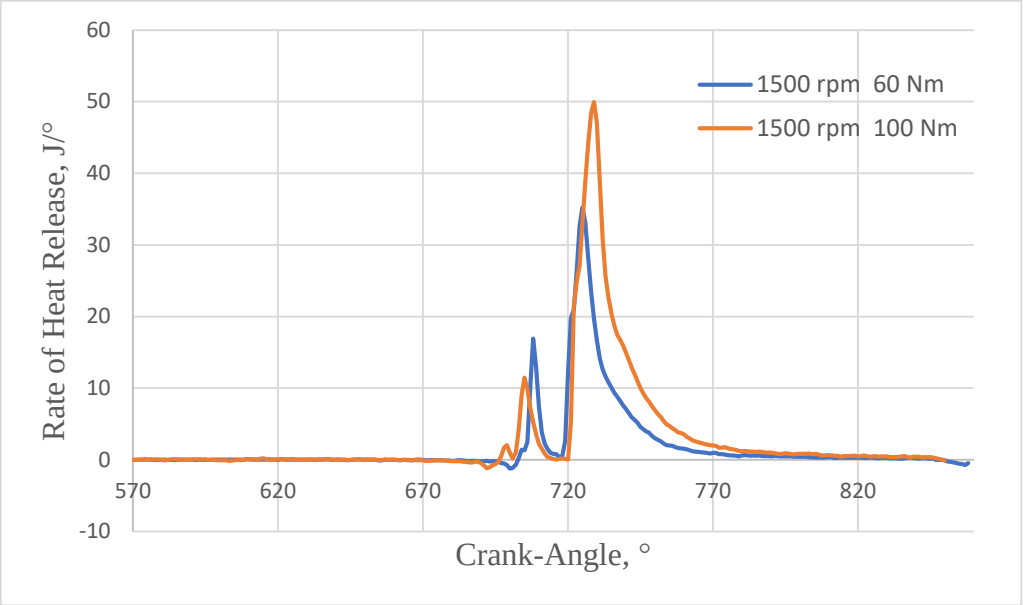

Figure 13 Rate of Heat Release from experimental research

3.1. Piston geometry

Piston geometry was provided with measurement data given by the Faculty of Mechanical Engineering in Ljubljana, and it is shown in Figure 14. Due to similarity with the small Greek letter ω, the piston type of experimental engine is called the ω shaped piston. 3D scan of the ω shaped piston geometry is shown in Figure 15.

Figure 14 Piston of the observed engine

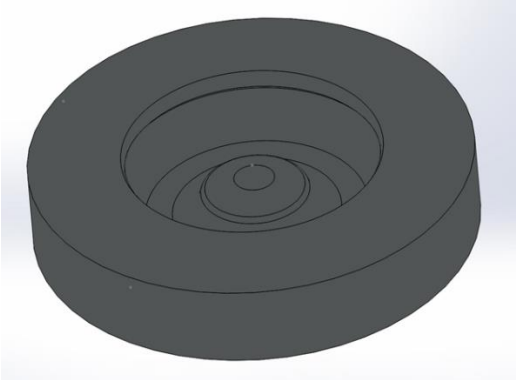

Figure 15 3D scan of the piston

When 3D scanner is not available, the alternative way of getting the piston geometry was tested. The 0.4 mm thick metal wire was shaped along the piston cylindrical contour. After shaping the wire, a scan of wires on the millimeter paper is made, as shown in Figure 16

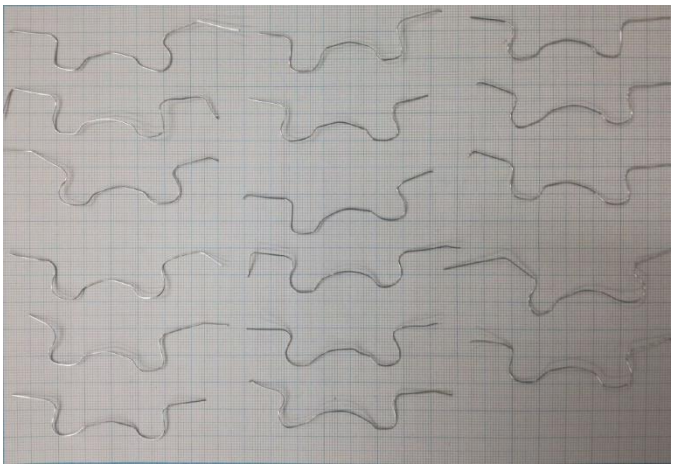

Figure 16 Wire to piston measurements

The piston is measured 34 times with 8 discarded measurements on a visual test. For other measurements coordination data of curves were made in software Engauge and after that data were interpolated with MATLAB code to the same value for getting the average curve.

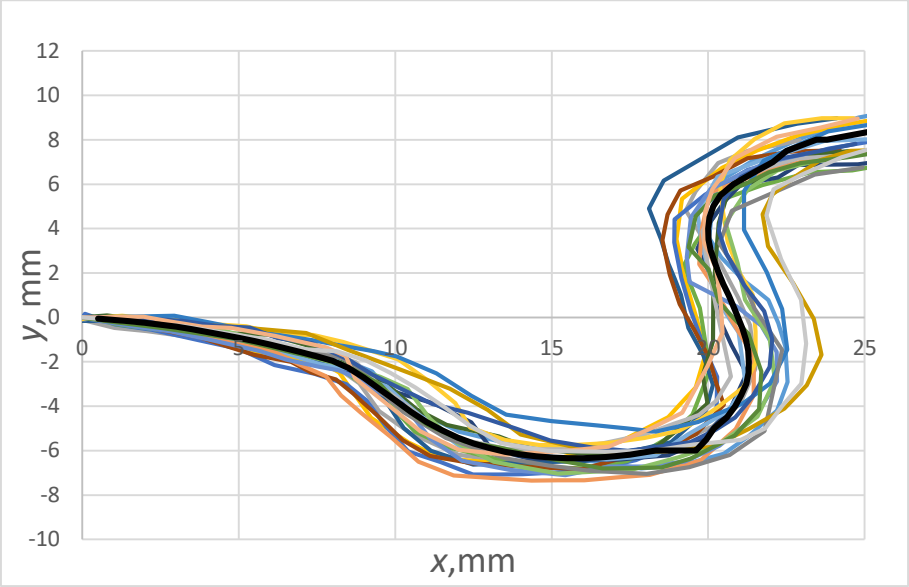

Figure 17 Wire to piston average curves

In Figure 17 the result of piston-wire measurement is shown, where every measurement is represented by one coloured curve. The calculated averaged piston shape curve is represented by the black curve. The difference between 3D scan, which has the most accurate values, and method with shaping wire is presented in Figure 18. Due to relatively big disagreements in measured piston shape, the piston geometry from the 3D scan was used for generating computational meshes.

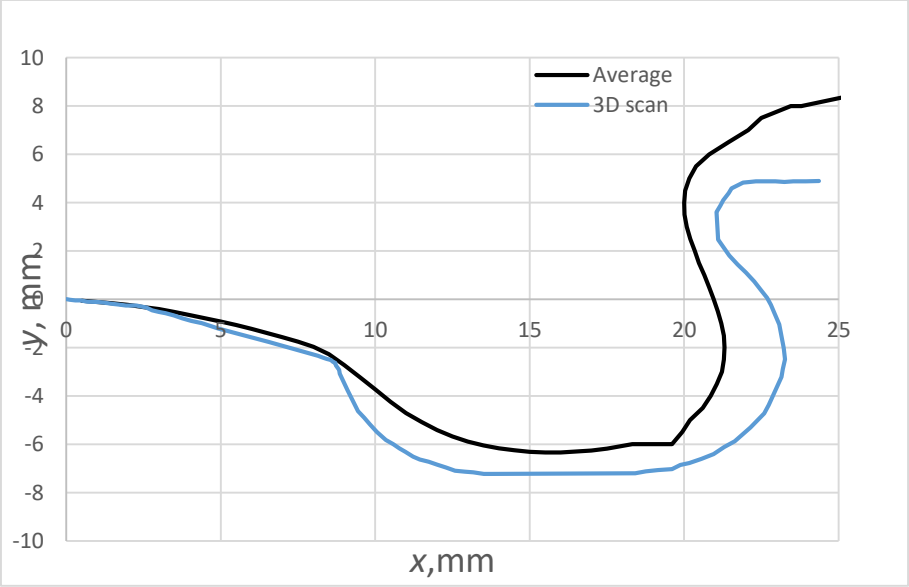

Figure 18 Comparison between 3D scan and average wire to piston curves

3.2. Injector

The injector position, dimension, pressure and nozzle dimension dictates the spray process during the fuel injection. Due to that, their properties are mainly provided by the manufacturer. The injector of experimental Diesel PSA 1.6 HDi engine is shown in Figure 19. Injector properties are presented in Table 4.

Figure 19 Injector of experimental engine

Table 4 Injector specifications

Number of holes	6
Hole diameter	0.115 mm
Spray Delta Angle	149 °
Needle diameter	4.0 mm, DLC coating (black)

3.3. Experimental data used for boundary conditions in CFD simulation

The piston temperature during engine working cycle was controlled by the oil, and the head temperature was controlled by the cooling water. Due to that, those surfaces were assumed as isothermal boundary conditions. Part of the experimental engine head with a smaller exhaust valve and the bigger intake valve is shown in Figure 20.

Diesel fuel used in the experiment is defined with norm EN 590. At the start of the compression stroke, the engine cylinder is filled with fresh air. There was no Exhaust Gas Recirculation (EGR). Experimental data for two engine operating conditions are presented in Table 5.

Figure 20 Cylinder head of experimental engine

Table 5 Experimental data for two engine operating points

Measure		1	2
Diesel fuel	Norm	EN 590	
Rotation frequency	min-1	1499.60	1500.18
Start and duration of the main injection	CA (°)	714	716
	μs	545	710
Injection pressure	bar	700	840
Start and duration of the pilot injection	CA (°)	695	687
	μs	240	280
Mass flow of Diesel fuel	kg/s	0.000623	0.000990
After compressor pressure	bar	11.702	12.600
Air temperature after intercooler	°C	51.25	43.26
Temperature of Diesel fuel	°C	17.81	19.11
Temperature of cooling water	°C	92.33	94.21
Temperature of oil	°C	<107.75	107.75

4. NUMERICAL SETUP

The numerical simulations were performed by using the commercial 3D Computational Fluid Dynamics (CFD) software AVL FIRE®. All simulations were performed using Euler Lagrangian approach for spray modelling. The gas phase is treated as the primary phase, and the injected liquid fuel parcels are treated as a secondary phase.

4.1. Meshes

Moving meshes were made using the commercial software AVL FIRE® ESE Diesel. Because injector has six nozzle holes, only one sixth of cylinder volume is used as a computational mesh. Different meshes were used in Case 1 and Case 2 but with similar block structure. Figure 21 shows the block structure of meshes used in both Cases. Both meshes are made mostly of hexahedron elements. The only difference between meshes is in compensation volume. The mesh used for Case 1 has a compensation volume at the piston, and the Case 2 mesh has a compensation volume at TDC clearance gap. The TDC compensation volume was generated as 0.34 mm extended clearance gap between the piston and head of the engine. In Case 1 mesh, TDC clearance gap was 1mm. Compensation volume is volume added to the original computational domain to realise actual compression ratio and to compensate all inconsistency in the geometry of the cylinder head.

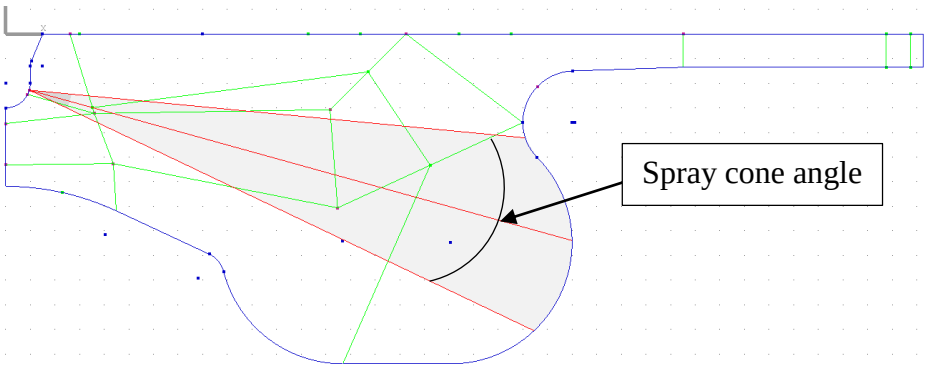

Figure 21 Block structure defined in ESE Diesel mesh generator

The only reason for creating Case 2 mesh is that the Case 2 had given irrational 3D results. Due to the earlier occurrence of the pilot injection (at 687°CA) some of the evaporated fuel was transported towards the compensation volume. Meshes used for Case 1 and Case 2 are shown

in Figure 22. In Figure 23, meshes at TDC and BTC are shown, whilst a total number of cells and number of generated meshes are defined in Table 6.

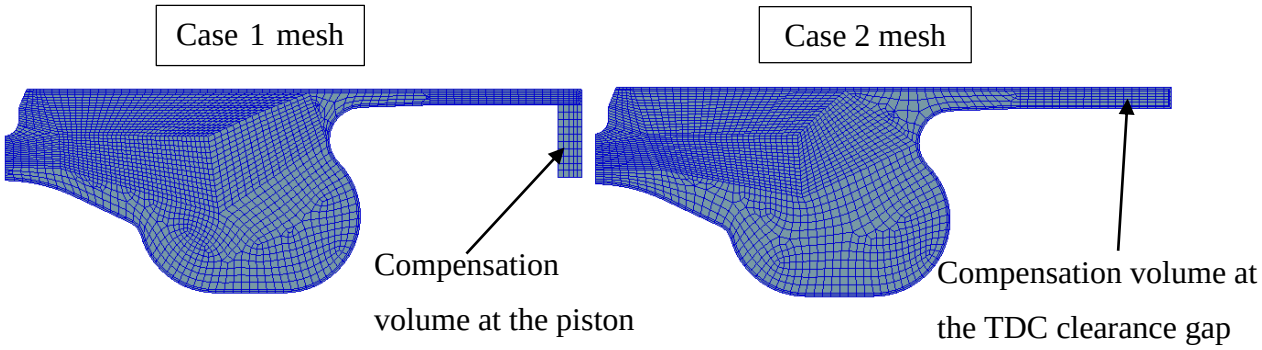

Figure 22 Generated computational meshes for Case 1 and Case 2

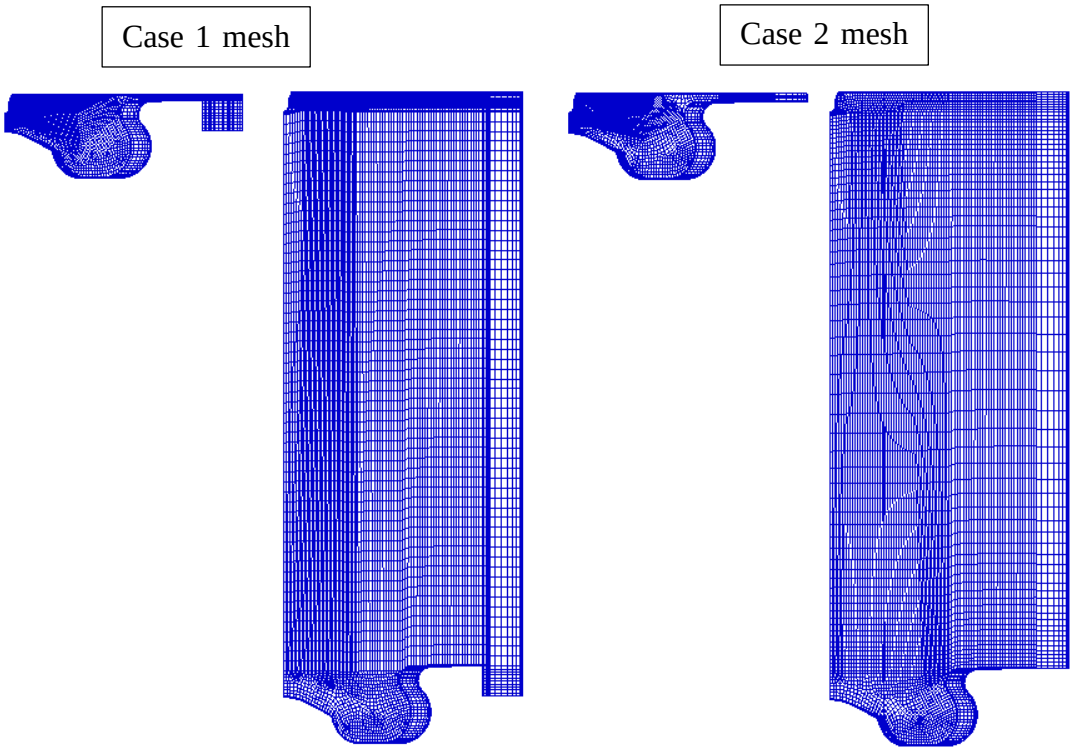

Figure 23 Case 1 mesh and Case 2 mesh topology at TDC and BDC

Table 6 Total number of cells at TDC and BDC

Mesh	Number of cells at TDC	Number of cells at BDC	Number of meshes
Case 1	44013	131427	21
Case 2	42041	117623	21

4.1.1. Mesh dependency test

Three meshes with same block structure, but with a different number of cells, were generated to test the impact of mesh resolution on the simulation results, as shown in Figure 24. The only parameter that was different in meshes was the average cell size. The mesh specifications are given in Table 7.

Table 7 Properties of the generated computational meshes

Mesh	**Average cell size, mm**	**Number of cells in TDC**	**Number of cells in BDC**	**Number of meshes**
Very fine	0.4	59857	182988	25
Fine	0.5	44013	131427	21
Medium	0.6	30277	81549	21

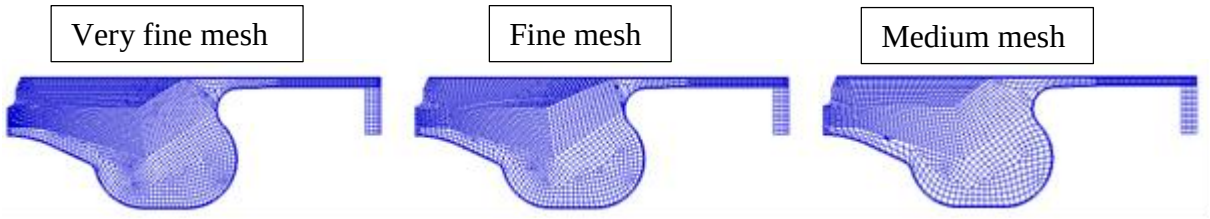

Figure 24 Computational meshes used for mesh dependency test

After the computational meshes were generated, the operating point Case 1 was calculated for each mesh. The results of mean pressure inside the cylinder are presented in Figure 25. The results in Figure 25 are shown from the start of pilot injection (695° CA) to the 740° CA, to gain a better visibility of calculated mean pressure curves. An agreement of numerical results for different meshes is shown in Figure 25. To conclude, the impact of mesh resolution on simulation results was minor. In the following simulations of Case 1, the fine mesh will be used. The mesh dependency test was not performed for the mesh used in Case 2 due to the same topology as mesh used in Case 1.

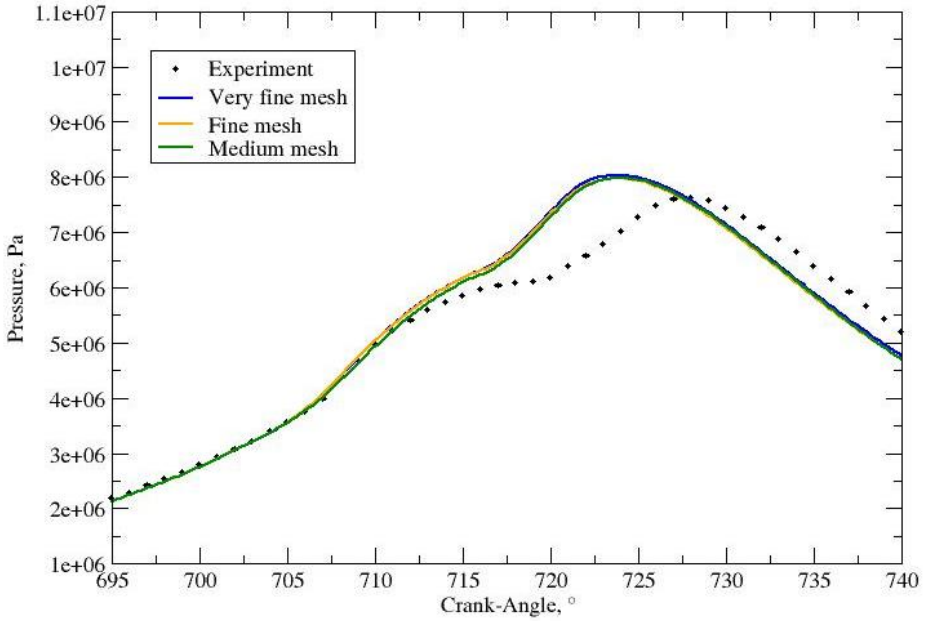

Figure 25 Impact of mesh cell size on mean pressure results

4.2. Time discretization

The period of the numerical simulation was same as the period of working cycle in experimental data. The inlet and exhaust valves were closed, during the period of working cycle in experimental data. The start of numerical simulation was set up to 570° CA, and the end was defined at 850° CA. Time step used in the simulation is shown in Table 8. The smaller time step is defined in the period of fuel injection, due to numerical stability.

Table 8 Simulation time step

Up to Crank-Angle, °	Time step, °
571	0.1
685	1
720	0.15
750	0.25
800	0.5
850	1

4.3. Boundary and initial conditions

Boundary conditions (BC) at the volume mesh were defined using face selections. Face selections of Case 1 mesh are shown in Figure 26 but the same methodology is used for Case 2. Isothermal boundary conditions were used for the cylinder head, piston and liner. The cylinder geometry was assumed to be symmetric around the cylinder axis and therefore, the segment boundary was periodic on the both sides of the mesh. Table 9 shows boundary conditions for the selections in Figure 26.

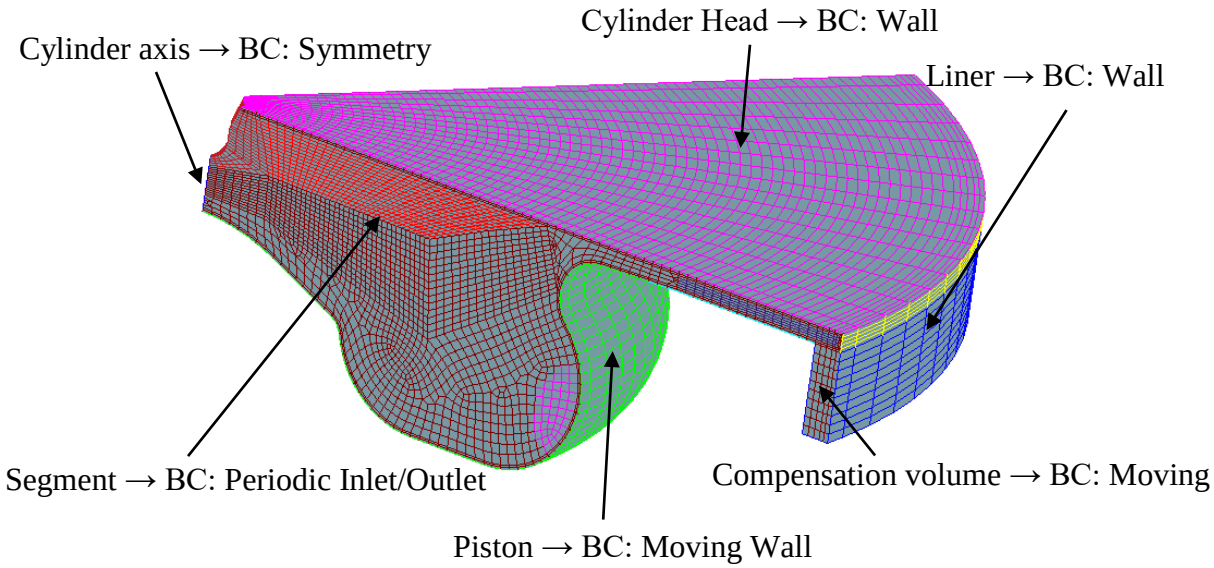

Figure 26 Boundary selections of the computational mesh

Table 9 Boundary condition for both cases

Piston temperature	160 °C
Head temperature	120 °C
Liner temperature	120 °C
Axis	Symmetry
Segment boundary	Boundary connection

Due to the defined compensation volume, Case 1 has additional adiabatic boundary condition at the walls of compensation volume. The boundary condition dependency test was performed changing a piston temperature. The impact of piston temperature was tested because the piston is the only boundary in contact with spray parcels. Figure 25 shows the impact of the piston

temperature on the Case 1 results. The agreement in curves demonstrates that the impact of piston temperature on simulation results is minor. Figure 25 has the same period as Figure 25, from the start of pilot injection (695° CA) to selected end of 740° CA.

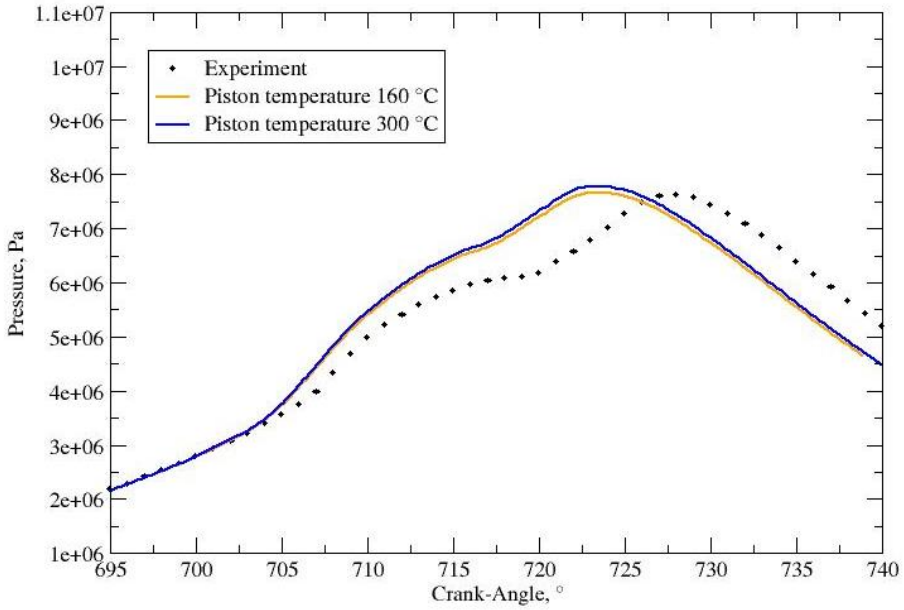

Figure 27 Impact of the piston temperature on the mean pressure

Besides the temperature and pressure initial conditions, the CFD simulations of IC engines requires the initial gas composition [24]. The initial gas composition is defined as the initial mass fractions of species inside the computational domain at the start of the simulation. Initial conditions are given in Table 10. Initial pressure and temperature value are taken from the available experimental data. At the start of the simulation, only the fresh air was defined inside the cylinder. Turbulence kinetic energy was selected as the default value in FIRE®, whilst the swirl value was defined with 2000 min^{-1}.

Table 10 Initial conditions for Case 1 and Case 2

	Case 1	Case 2
Pressure	1.18	1.245
Temperature	373.343	341.872
Gas composition	fresh air	fresh air
Turbulent kinetic energy	0.001	0.001
Swirl	2000	2000

4.4. Solver control

Underrelaxation factor expresses how much of calculated value from the last iteration would be taken in the next iteration. The underrelaxation factor is limited to ensure the convergence of results. Table 11 shows the underrelaxation factors used in the simulation.

Table 11 Underrelaxation factors

Momentum	0.6
Pressure	0.5
Turbulent kinetic energy	0.4
Turbulent dissipation rate	0.4
Energy	0.95
Mass source	1
Viscosity	1
Scalar	0.8
Species transport equations	0.95

Differencing schemes

The central differencing scheme was used for momentum and continuity balances, whilst the upwind differencing scheme was used for turbulence, energy and scalar transport equations. The solution was converged when the pressure residual decreased under the 10^{-5}.

4.5. Spray setup

Spray module contains all parameters for spray simulation. Firstly, the fuel properties were selected where the properties of Diesel EN590 are already implemented in FIRE®. The temperature of injected fuel was measured in the experimental research and it was defined by 20 °C. The density of fuel at injection temperature was defined with 820 kgm^{-3}. After the liquid properties were defined the selection of sub-models followed. Sub-models used in the numerical simulation are given in Table 12.

Table 12 Sub-models

Drag law model	Schiller-Naumann
Turbulent dispersion model	Enable
Wall Interaction model	Walljet1
Evaporation model	Dukowicz (E1 = 1; E2 = 1)
Breakup model	WAVE
Turbulence model	k-zeta-f

After that, the size of different parcels and the injection location of parcels from on the nozzle hole were selected. Table 13 shows selected parameters in FIRE® for Euler Lagrangian spray simulation.

Table 13 Particle introduction from nozzle

Number of different particle sizes introduce per time step and radius	3
Number of radial parcels release location on nozzle hole	6
Number of circular parcels release location on each radial parcel	6

The injector geometry required for simulation was measured or taken over by the manufacturer. Table 14 shows the injector data required for numerical simulation. Spray angle delta 1 in Table 14 is the double angle between the spray axis and nozzle axis. The initial size of parcels that are injected in the domain is equal to the nozzle hole diameter.

Table 14 Injector geometry

Position	(0, 0, -2.28) mm
Direction	(0, 0, 1)
Spray angle delta 1	149°
Nozzle diameter at hole centre position	2.05 mm
Nozzle hole diameter	0.115 mm

The angle between the nozzle hole axis and the widest parcel trajectory is required for simulation, and it is called the half outer cone angle. The half outer cone angle was calculated according to next expression [26]:

$$half\ outter\ cone\ angle = arctg\left[\frac{4\pi\sqrt{3}}{6\left(3+0.28\left(\frac{l}{d_{nh}}\right)\right)}\sqrt{\frac{\rho_g}{\rho_f}}\right] \tag{50}$$

where l is the length of the nozzle, and d_{nh} is the nozzle hole diameter. Half outer spray angle was calculated from equation (50), where the impact of l was neglected due to its small influence on total value. Also, the length of nozzle had not been provided by the injector manufacturer. In the pilot injection half outer spray angle was set up to 10° and in the main injection was 7°, for both modelling cases.

Injection rate

Mass injected into one working cycle is calculated from the total fuel consumption. The total fuel consumption was measured at the fuel tank. The connection between those two values is obtained from mass conservation law, and can be expressed as:

$$m_{\text{cycle}} = \frac{\dot{m}_{ft}}{f \cdot n_{cycl} \cdot n_{nh}} \tag{51}$$

where $\dot{m}_{ft}$ is fuel consumption, f is the engine speed (rotation per s), n_{cycl} number of cylinder that engine has (4), and n_{nh} is number of nozzle holes that injector has (6). The number of nozzle holes directly indicate affect the volume of computational domain. One complication is that simulation of that exact mass injected during pilot injection is not known, only total mass of both injections is known. Table 15 shows the duration of the pilot and main injections and the selected mass distribution between injections. The injection rate in experiment is also not known, so standard rectangle shape was assumed.

Table 15 Pilot and main injection data

	CASE 1	CASE 2
Pilot mass	0.5 mg	0.8 mg
Total mass	2.077 mg	3.3 mg
Pilot start	695°CA	687°CA
Main start	714°CA	716°CA

Figure 26 and 27 show assumed rectangular injection rate. The ratio of mass flows between Case 1 and 2 are equivalent. The impact of mass injected in pilot injection will be shown in the following chapter.

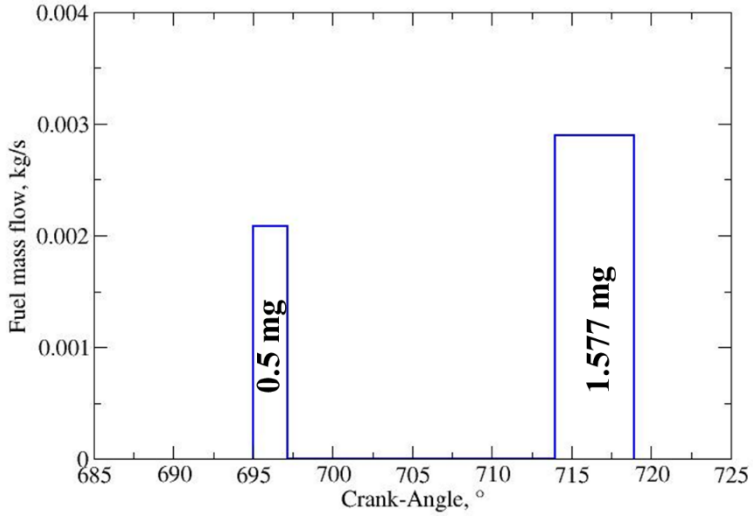

Figure 28 Case 1 injection rate

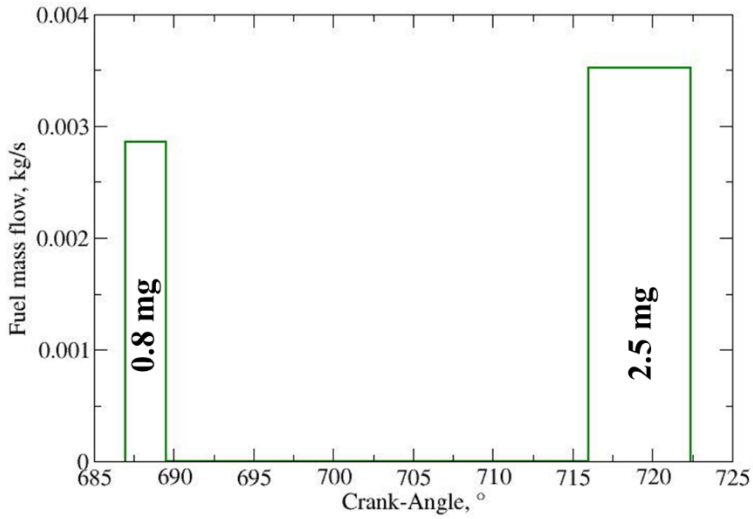

Figure 29 Case 2 injection rate

Other assumptions used in numerical simulations:

- Air had ideal gas properties: Prandtl number, Pr = 0.9 and Schmidt number, Sc = 0.9
- Compressible flow
- Viscid fuel (WAVE C_3 = 1)
- No interaction between droplets
- No water vapour in air

5. RESULTS AND DISCUSSION

In the previous chapter, all input data for numerical simulations was presented. In this section, the impact of swirl motion, pilot injected mass, and impact of WAVE constant C_2 on in-cylinder thermodynamic state is analysed. The process of selecting suitable parameters is called the spray calibration, and it is the standard procedure of the spray simulation. The results with the chosen parameter set are presented and the comparison between two simulations is shown. The combustion model ECFM 3Z+ and n-heptane chemical mechanism were used to calculate the combustion process. Finally, the comparison of Case 1 and 2 is performed.

5.1. Impact of swirl motion

In chapter 1.2.1., function of the swirl motion in Diesel engines was described. Since the value and direction of the swirl motion inside the cylinder for the experimental engine were not provided, the impact of swirl was investigated. In addition, the geometry of the inlet valve ports was not known and the swirl number could not be obtained from the cold flow simulation of air through the intake ports. From the literature, swirl value for DI Diesel engines in bowl-in pistons goes up to 4000 rpm [9]. Therefore, to test the swirl influence on the mean pressure two cases were calculated with different values of swirl: 2000 rpm and 0. Figure 30 shows the results of swirl influence. The light blue vertical lines in Figure 30 present the period of injections, where PI means pilot injection and the MI mass injection. For the observed engine, the swirl does not have a significant impact on the in-cylinder mean pressure. Therefore, the swirl was defined with a value of 2000 rpm. It is important to accentuate that the impact of swirl motion had to be tested, due to its impact in many cases, such as in the numerical simulation of emissions [12].

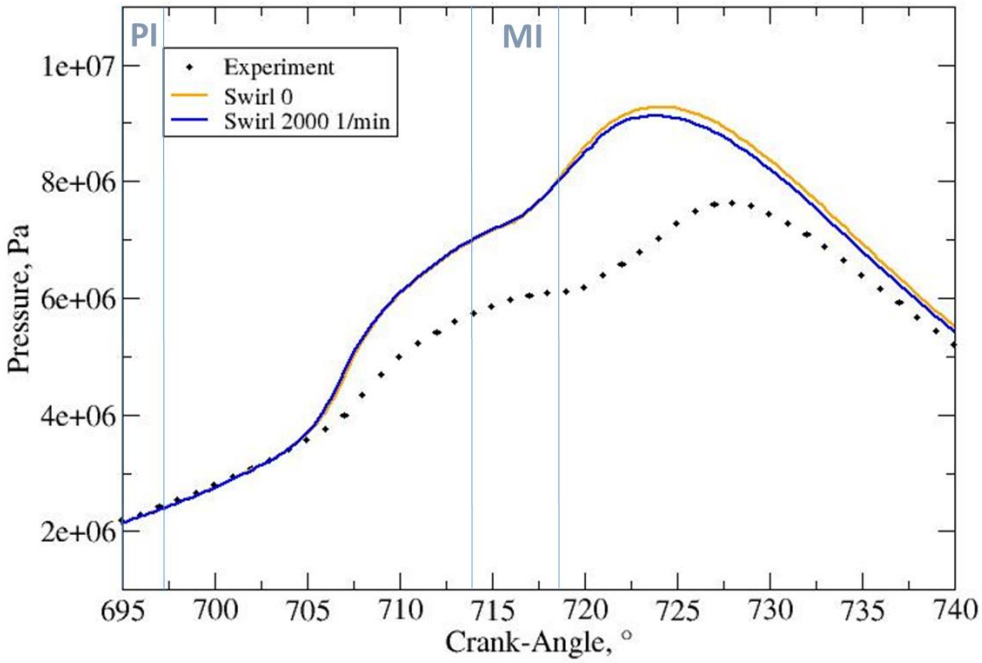

Figure 30 Impact of the swirl motion on the mean pressure for Case 1

5.2. Impact of fuel distribution between pilot and main injections

In the observed experimental engine, there were two separated injections, called the pilot and main injections. Multi-injection system is effective in reducing emissions and combustion noise [18]. In the observed cases, only the overall engine fuel consumption was known, as shown in Table 5. This consumption is used to calculate the total mass injected in the single working cycle. The fuel mass injected in the pilot injection was an unknown. Therefore, shifting of fuel mass between injections was performed. For the first testing case, the pilot injected fuel mass was set up to 0.3 mg. The orange curve in Figure 31 shows the mean pressure results of such a case. The light blue vertical lines in Figure 31 present the period of injections, where PI means pilot injection and the MI mass injection. When combustion of the vapour produced due to the pilot injection, the pressure values are lower than experimental data. Due to that fact, in the next simulation case, more fuel was injected through the pilot injection process. The blue curve in Figure 31 shows a good agreement with the experimental data. The green line in Figure 31 present the last simulation case where even more mass was injected with the pilot injection (0.7 mg). The last simulation case provided the highest pressure after pilot injection since the more fuel is burned in this period. Also, the last case has maximum pressure after the main injection

due to faster evaporation and combustion processes. As the result of this investigation, in the following simulations, 0.5 mg of liquid fuel was injected with the pilot injection.

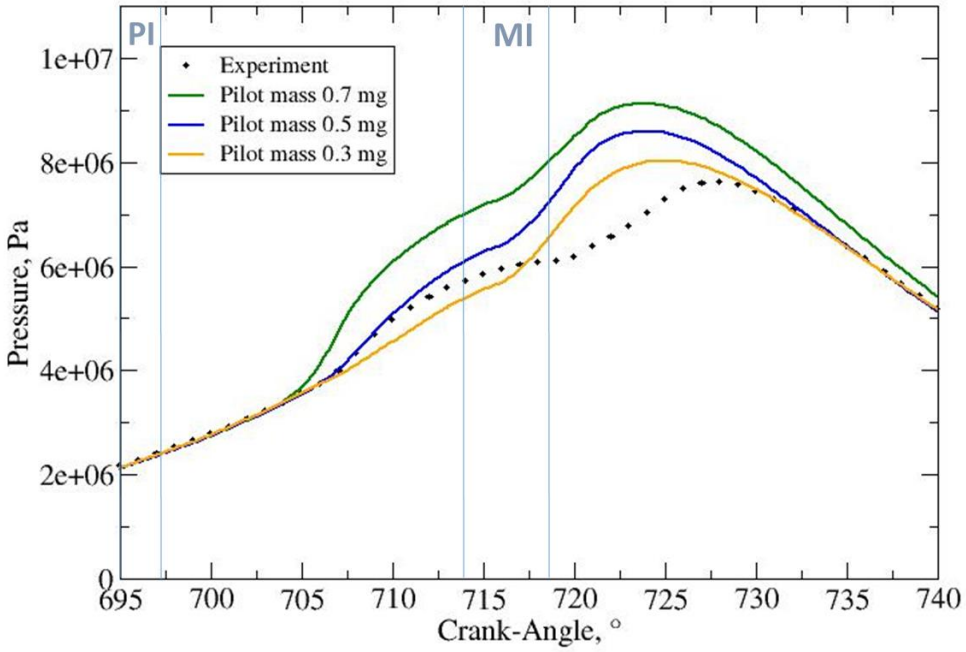

Figure 31 Impact of injected mass between PI and MI for Case 1

5.3. Impact of WAVE constant C_2

In chapter 2.3.1., the mathematical model of WAVE breakup model was presented. WAVE constant C2 defined in equation (29) influences droplet breakup time. Due to that, it is commonly used for calibrating simulation for different nozzles. Figure 32 shows mean pressure results of three testing cases with different modelling constant C2. If the value of WAVE C2 constant decreases, the breakup time of droplets will decrease. In Figure 32 the maximum pressure occurs for the lower values of C2. The lower breakup time increases the number of small diameter droplets, which have a bigger surface available for the heat exchange. With a larger surface, the evaporation of the fuel is faster. In Figure 32, C2 constant varied from 10 to 30. The combustion of main injection fuel occurs before the combustion in the experimental data, which could be addressed to a fast breakup of droplets in the main injection. That is why the C2 constant was assumed to be different for the pilot and main injection. A higher value in the main injection was selected to get longer breakup time, comparing to the pilot injection. Such a small change in C2 value has the significant impact on the mean pressure results, which

makes this case depend on constant C2. As the result of this investigation, in the following simulations, the C2 was defined with a value of 15 for PI and with 25 for MI.

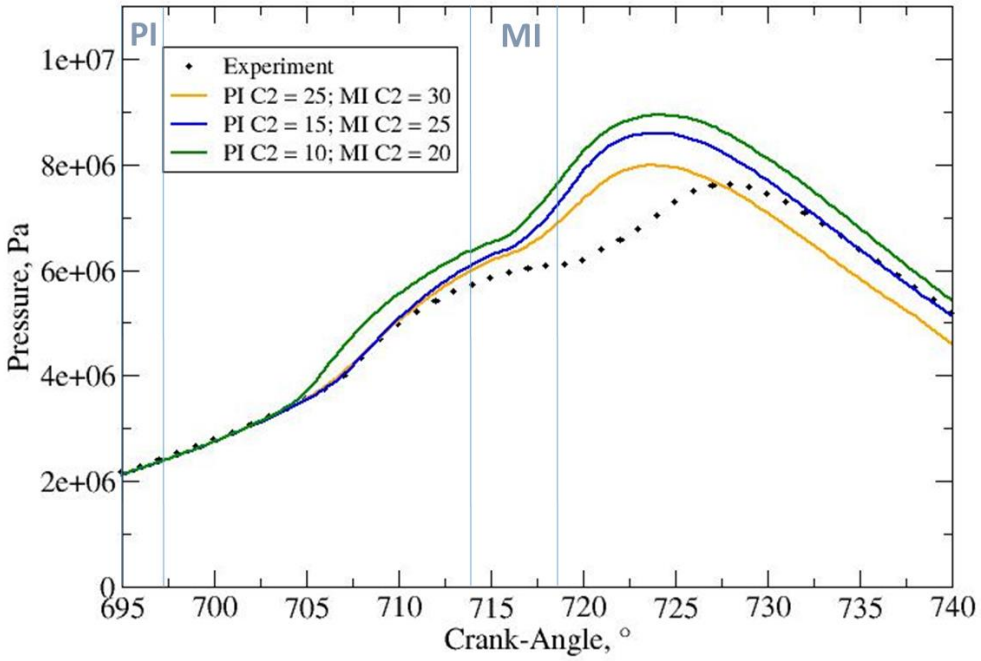

Figure 32 Impact of WAVE constant C_2 on the mean pressure for Case 1

5.4. Comparison between combustion model and chemical mechanism

In this chapter, the results obtained for Case 1 are presented. All 3D results were made for the cut section at the symmetry plane of the computational domain. Figure 33 shows the mesh and plane section used for 3D results. Figure 34 shows 3D spray results of the fuel injection into the cylinder. The size and colour of parcels represent the droplet diameter. At the start of injection, parcels are the same size as the nozzle hole diameter. Due to a high injection velocity, the parcels are broken into smaller ones.

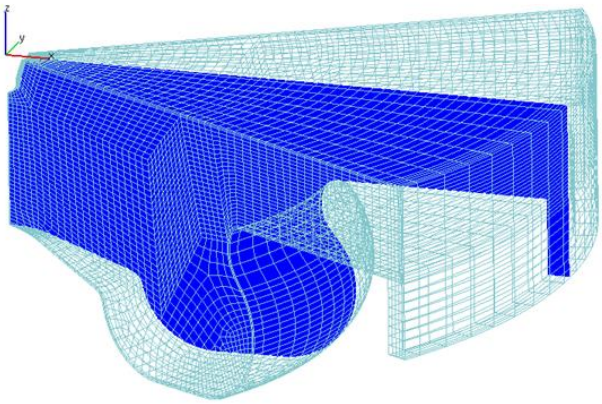

Figure 33 Cut section of the computational domain

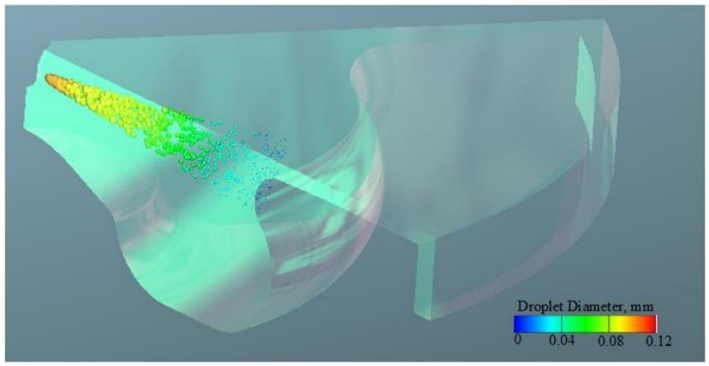

Figure 34 Injection of Lagrangian parcels into the engine cylinder

The combustion model used in all simulations was Coherent Flame Model, ECFM 3Z+. The chemical mechanism used in the numerical simulation was n-heptane C_7H_{16} mechanism considering 57 different chemical species and 293 chemical reactions. The calculation time with chemical mechanism is significantly increased due to time spent on the calculation of every species transport equation and DVODE solver. Figure 35 shows the difference in calculated mean pressure curve obtained by the combustion model and chemical mechanism. The results of chemical mechanism were calculated with the same spray parameters as in the combustion model. During the entire time of simulation, the results of mean pressure obtained with the chemical mechanism show higher values than the results obtained with the combustion model.

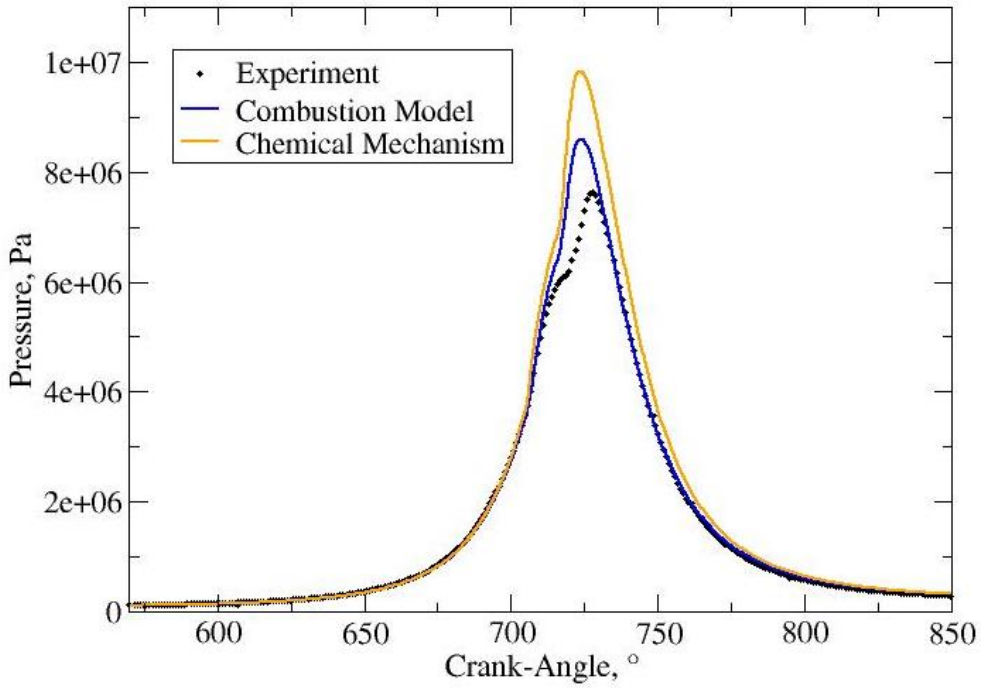

Figure 35 Mean pressure results for Case 1

The occurrence of the combustion process is also evident in Figure 36 that shows the calculated temperature results compared to the experimental data. Moreover, the inflexion points are in an agreement in Figures 35 and 36, since the mean temperature was calculated from the mean pressure data. The first inflexion point visible around 705° CA is the start of pilot mass combustion. The mean pressure gradient slightly increases from the compression process until the point around 705 °C when the heat from the chemical energy of the fuel is released. Another inflexion point is around 720° CA when the combustion of vapour produced from the fuel injected in the main injection occurs.

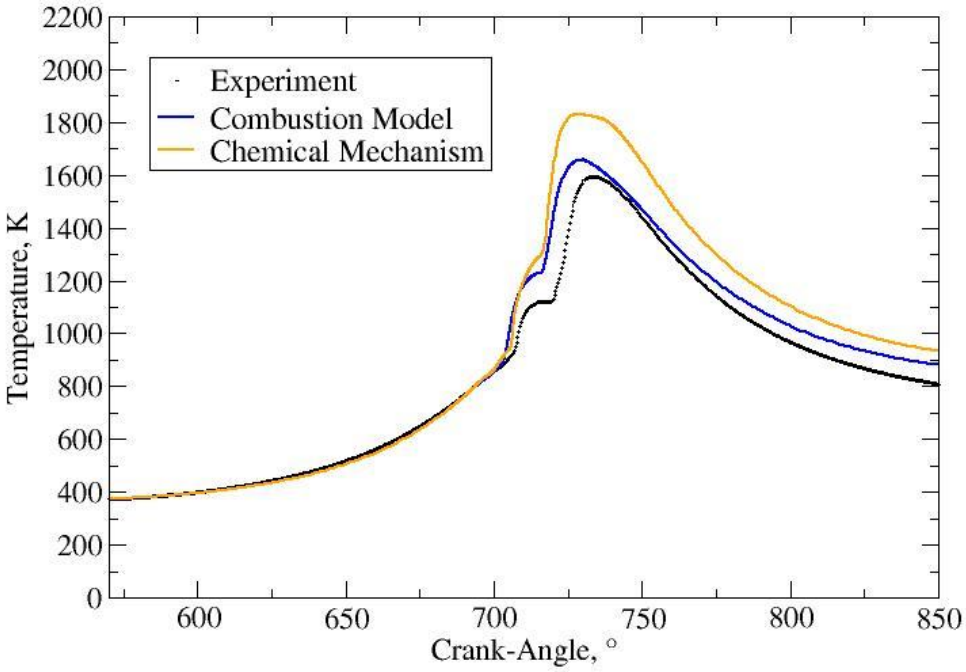

Figure 36 Mean temperature results for Case 1

Figure 37 shows the comparison of the experimental and calculated rate of heat release where the area under curves is the released energy. The time difference between the start of injection and the ignition point is called the ignition delay. Figures 35, 36 and 37 show the good agreement of pilot injection ignition delays between results and experimental data.

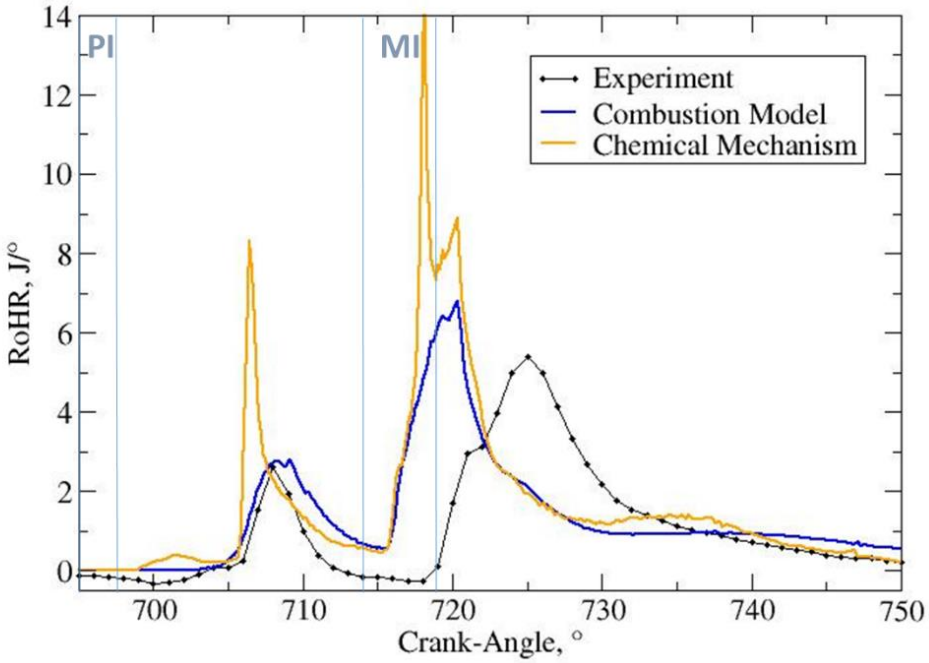

Figure 37 The rate of heat release results for Case 1

Figure 38 shows the temperature field during the injections for the cut section shown in Figure 33. On the left-hand side, the results obtained with the combustion model are shown. On the right-hand side, the results of the n-heptane mechanism for the same °CA are shown. The first temperature field at 696° CA shows the pilot injection. The cooling of the gas phase is visible, due to the lower temperature of injected fuel (20 °C) and the evaporation process. At 710° CA, the combustion of pilot mass occurs, and the rise in temperature is visible at the combustion regions. At the 715°CA, the main injection occurs, which is demonstrated again with a lower temperature in spray region. This region is more visible at the combustion model since the mean temperature is lower in that case. The peak temperature is recorded at 725° CA, where the maximum temperature is higher in chemical mechanism than in combustion model. The higher temperature in the chemical mechanism can also be seen from 2D results in Figure 38. The results at 737° CA shows the temperature decrease due to a gas expansion.

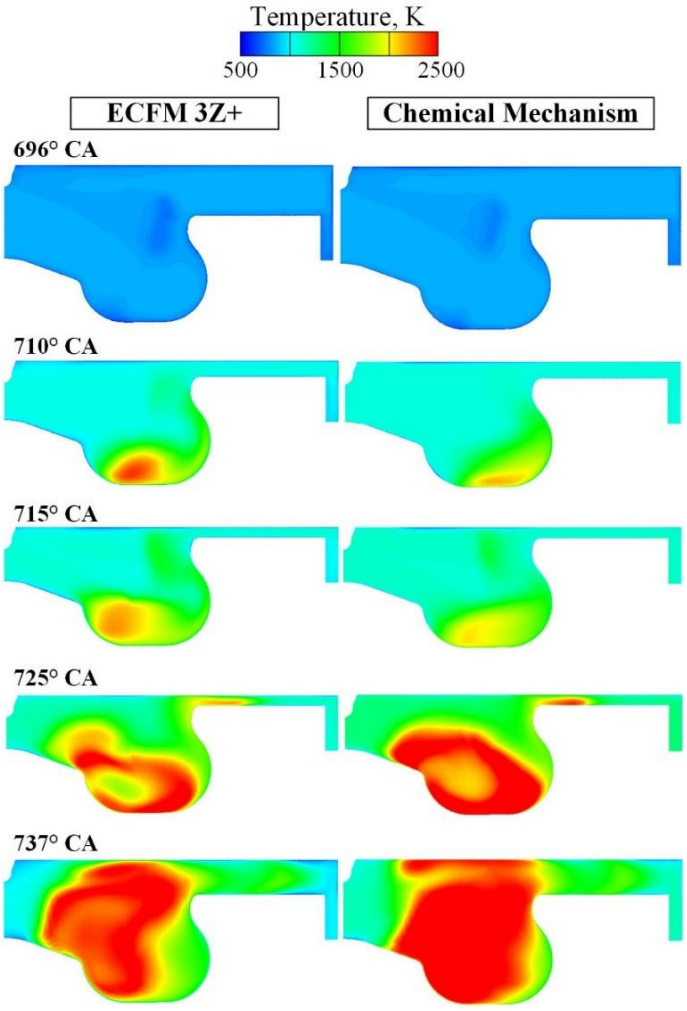

Figure 38 Temperature field inside the cylinder

Figure 39 shows the evaporated fuel field and spray parcels during and after the pilot injection. The liquid parcels are coloured with their diameter. As it was shown in Figure 38, the combustion model results are on the left-hand side, and the chemical mechanism results are on the right-hand side. The results recorded at 696° CA show the fuel pilot injection process. The mass fraction of the evaporated fuel is the highest where the droplet particles are the smallest. The pilot injected fuel was faster evaporated in ECFM 3Z+ simulation case, rather than in simulation case where the chemical mechanism was used. At the 698° CA, the pilot injection ended, and only the smallest droplets remained in the cylinder. The calculated vapour cloud is in a good agreement between the observed Cases. At crank angle position of 706° CA, the remaining evaporated fuel is shown. The less remaining evaporated fuel in n-heptane mechanism could be addressed to a faster combustion process.

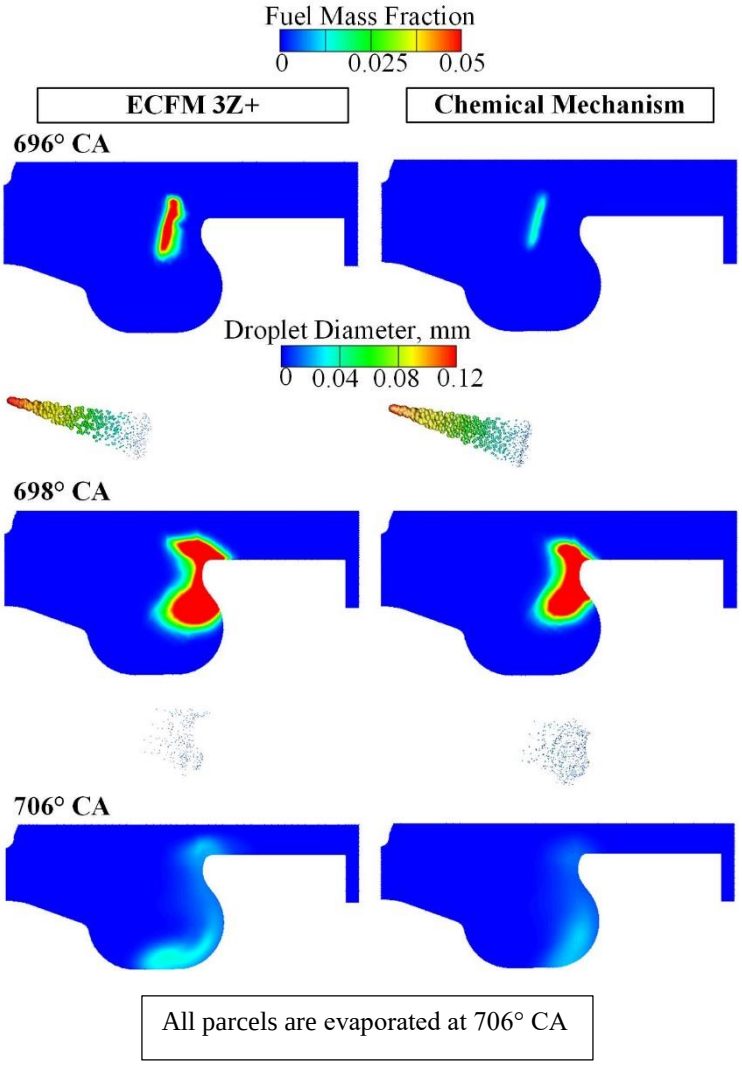

Figure 39 Evaporated fuel and spray parcels during the pilot injection

Figure 40 shows the evaporated fuel field and spray during the main injection, it is also the extension of Figure 39. Two parameters were different in the main injection comparing to the pilot injection. The spray angle was lowered, and WAVE constant C_2 was higher (the breakup time of droplets was extended). In addition, the injected mass was larger in the main injection. As expected, the results are qualitatively similar to results recorded in the pilot injection. The region of evaporated fuel in ECFM 3Z+ is slightly bigger than in chemical mechanism during the observed simulation period.

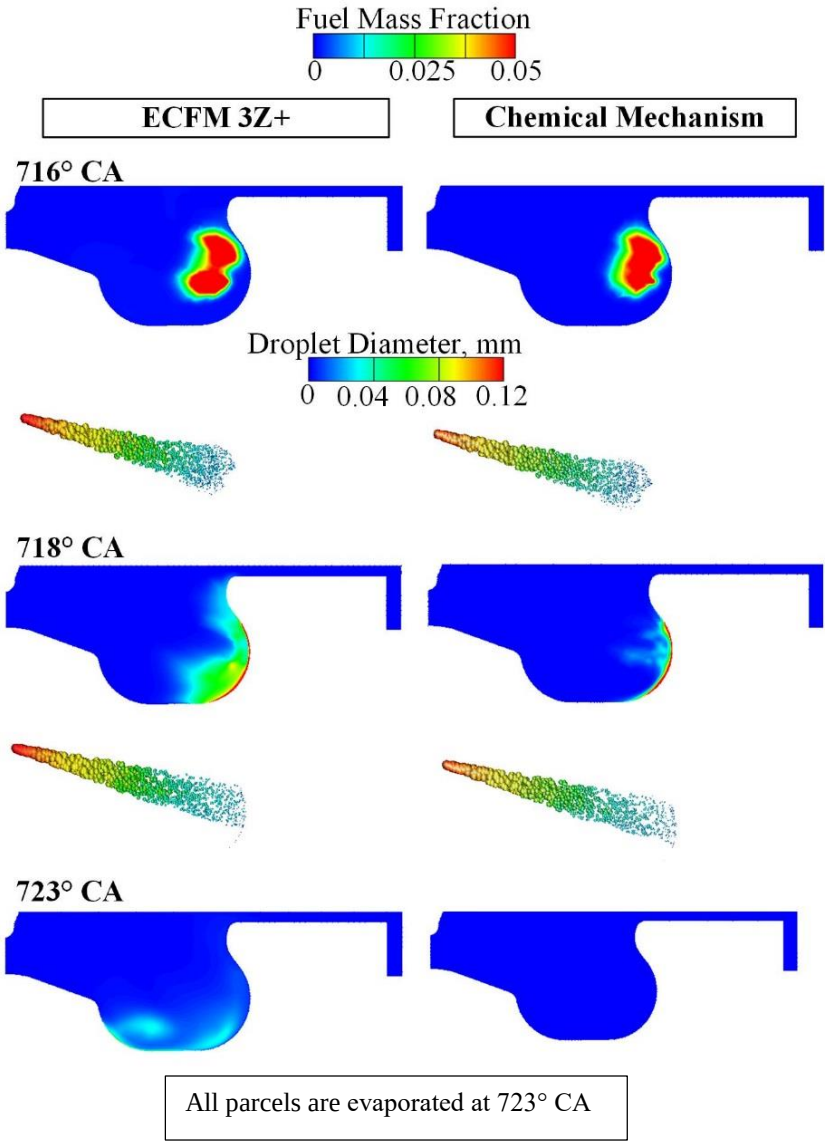

Figure 40 Evaporated fuel and spray parcels during the main injection

5.5. Case 2 results

In this chapter, the 2D results for Case 2 are presented. The main difference between Case 1 and 2 are the bigger total fuel injected mass in the Case 2, and the timing of injections. The injection rate of the Case 2 was shown in Figure 29. All parameters of spray sub-models in Case 2 were taken from the Case 1. In the Case 2, the ECFM 3Z+ combustion model was used. Figure 41 shows the difference between the calculated and experimental mean pressure. During the compression stroke, the calculated mean pressure is lower than the experimental data. However, after the combustion starts, the calculated mean pressure is higher than the experimental results as shown in Figure 41. The deviation of calculated curves from experimental data could be reduced by tuning the spray parameters particularly for Case 2.

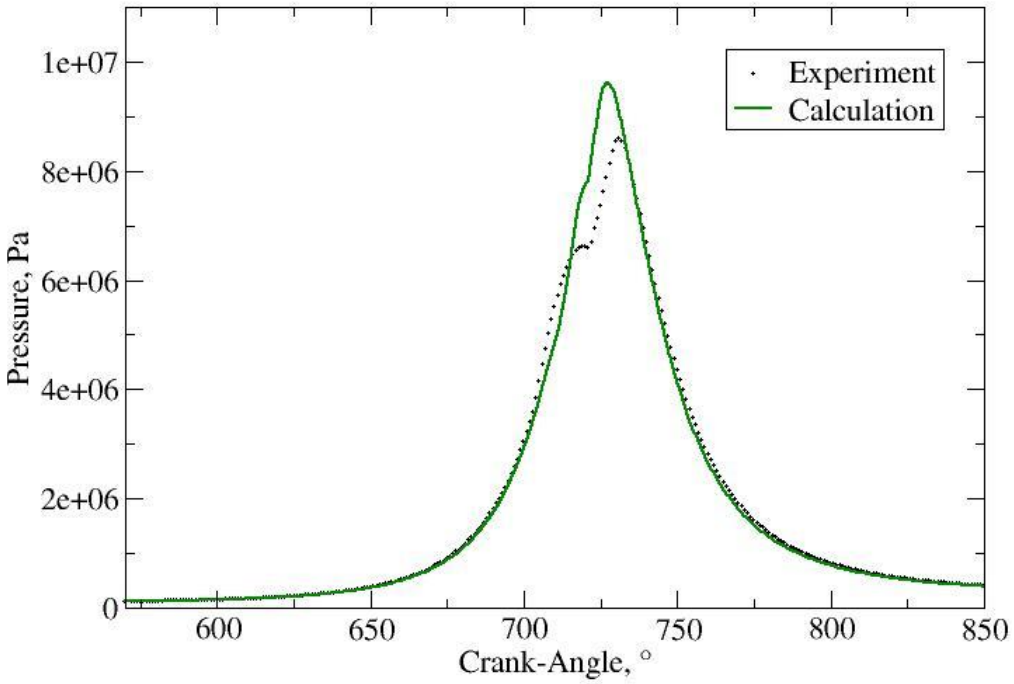

Figure 41 Mean pressure results of Case 2

The ignition of pilot fuel is around 705° CA, and it is less emphasised than in the Case 1. The Case 2 ignition delay is higher than in the Case 1, which could be addressed to more injected fuel. The time necessary for evaporation of the injected fuel increases with the increase of injected fuel mass. In Figure 41, the ignition of evaporated fuel from the pilot injection does not increase a gradient of the pressure curve. That is probably due to a smaller mass injected in the pilot injection. The ignition of fuel evaporated in the main injection occurs in the middle of

the main injection, and it is visible at temperature curve in Figure 42. In Figure 42, the gradient of the temperature curve is similar as in experimental data. That is opposite of the mean pressure results, where the gradients are different. The pressure results indicate that too much mass is dedicated to the main injection, whilst the temperature results suggest that this mass is correctly chosen.

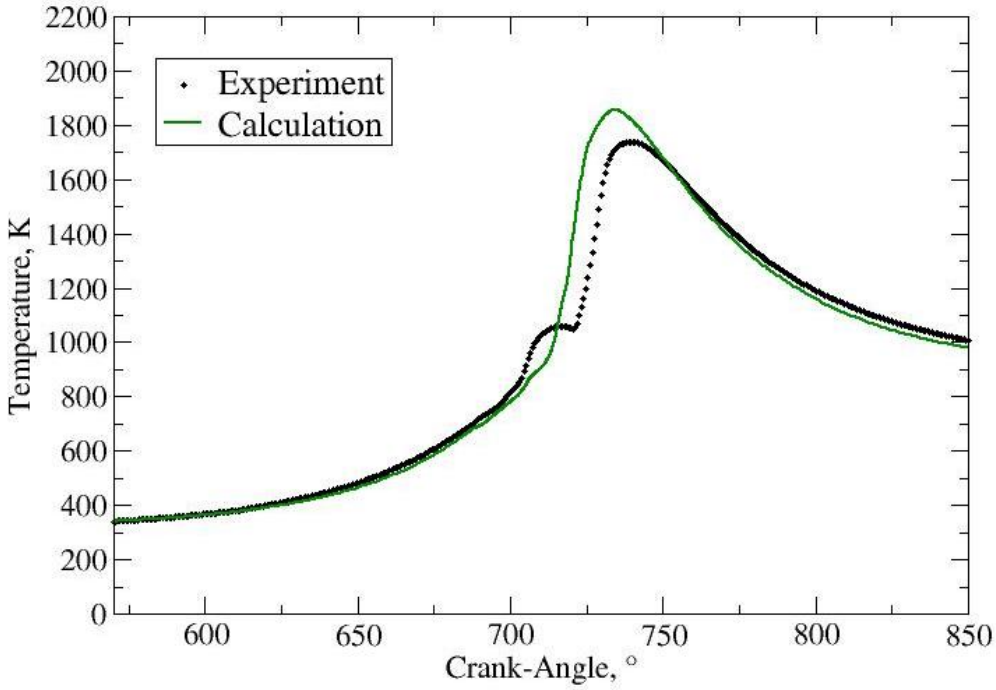

Figure 42 Mean temperature results for Case 2

Figure 43 shows the rate of heat release, which indicates that the mass dedicated to the pilot injection is too small. The area under the calculation curve is smaller than area calculated from the experimental data meaning that the lower amount of energy is released in the combustion process. The ignition of fuel evaporated in the main injection is too fast in comparison with experimental data. The time-dependent injection rate profile with lower injected mass at the start of the injection could be examined for solving that problem. To conclude, it is possible that some other values of sub-model coefficients may give more accurate results for this specific case.

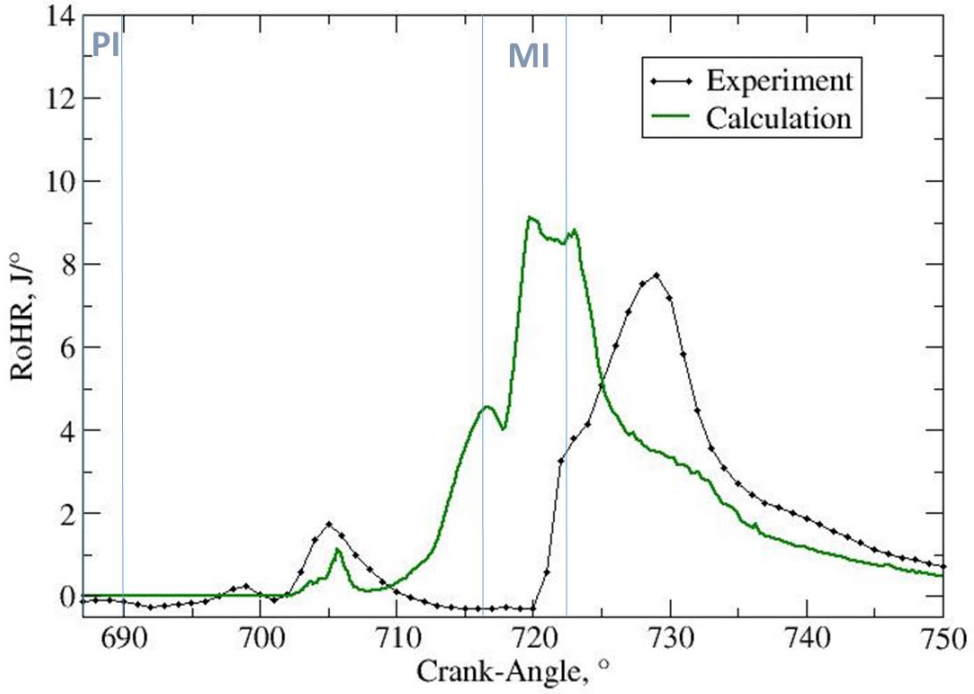

Figure 43 The rate of heat release results for Case 2

5.6. Comparison between Case 1 and Case 2

In this chapter, the comparison of Case 1 and Case 2 3D results are presented. Figure 44 shows the gas phase temperature field during the injection and combustion processes for the cut section shown in Figure 33. On the left-hand side, the Case 1 results are shown. On the other side, the Case 2 results at the equivalent moment are shown. Since the Case 1 and Case 2 have different injection time, comparison of the results at the same °CA has no sense. The first temperature fields recorded at 697°CA and 688° CA show the influence of the pilot injection on the local temperature. The lower temperature in the spray region could be addressed to the lower fuel temperature (20 °C) and to the evaporation process.

At the crank angle position of 713° CA and 714 °CA, the combustion of evaporated fuel is in the progress. The different combustion regions of Case 1 and 2 are shown. Some of the evaporated fuel in Case 2 went into the TDC compensation volume. Moreover, that is why the different mesh was generated for Case 2. If the simulation of Case 2 was performed on the Case 1 mesh, the evaporated fuel would go in the compensation volume at the piston. That would lead to the unphysical results because the compensation volume at the piston does not exist in the engine. At 716° CA and 718° CA the similar temperature distribution in spray region is

shown for in both cases. The hot gas regions inside the cylinder are different due to differences in the pilot injection process. In Case 1 a higher temperature region was recorded in the bowl of the piston, whilst in the Case 2, the high temperature is noticeable in TDC compensation volume. That is a possible reason for the lower temperature results in Case 2. Finally, after the main injection, the combustion of the remaining vapour occurs at 717° CA and 720° CA. where the results of Case 2 are similar to the results in Case 1.

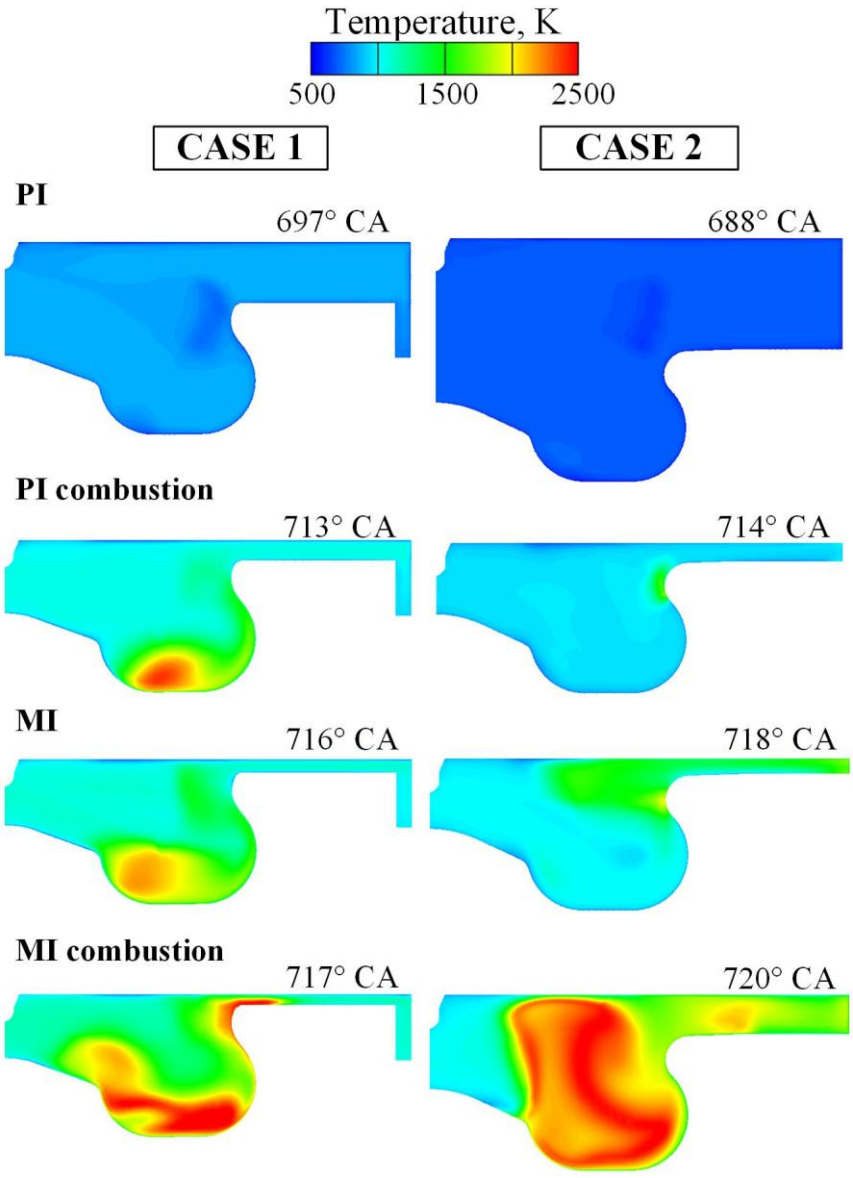

Figure 44 Comparison of temperatures fields in Case 1 and 2

Figure 45 shows the evaporated fuel field during and after multi-injections. Similarly, to results shown in Figure 44, the Case 1 results are placed on the left-hand side, and the Case 2 results

are on the right-hand side. The first evaporated fuel fields recorded at 697°CA and 688° CA, when the pilot injection occurs, show the faster evaporation process in Case 1 than in Case 2, due to a smaller injected mass and a higher temperature of surrounding gas. After the pilot injection, at 701° CA and 690° CA, the most of the evaporated fuel in Case 2 went into the TDC compensation volume. Case 2 shows a higher mass fraction of the evaporated fuel after the pilot injection, comparing to the Case 1. At the crank angle position of 713° CA and 714 °CA, the main injection occurs. Case 1 shows that all evaporated fuel of pilot injection is burned, comparing to the Case 2, where the evaporated fuel of pilot injection is still in the cylinder. Finally, after the main injection, the combustion of the remaining evaporated fuel occurs at 719° CA and 722° CA. The results of Case 2 are similar to the results in Case 1 since the evaporated fuel of the main injection is not inside the TDC clearance gaps.

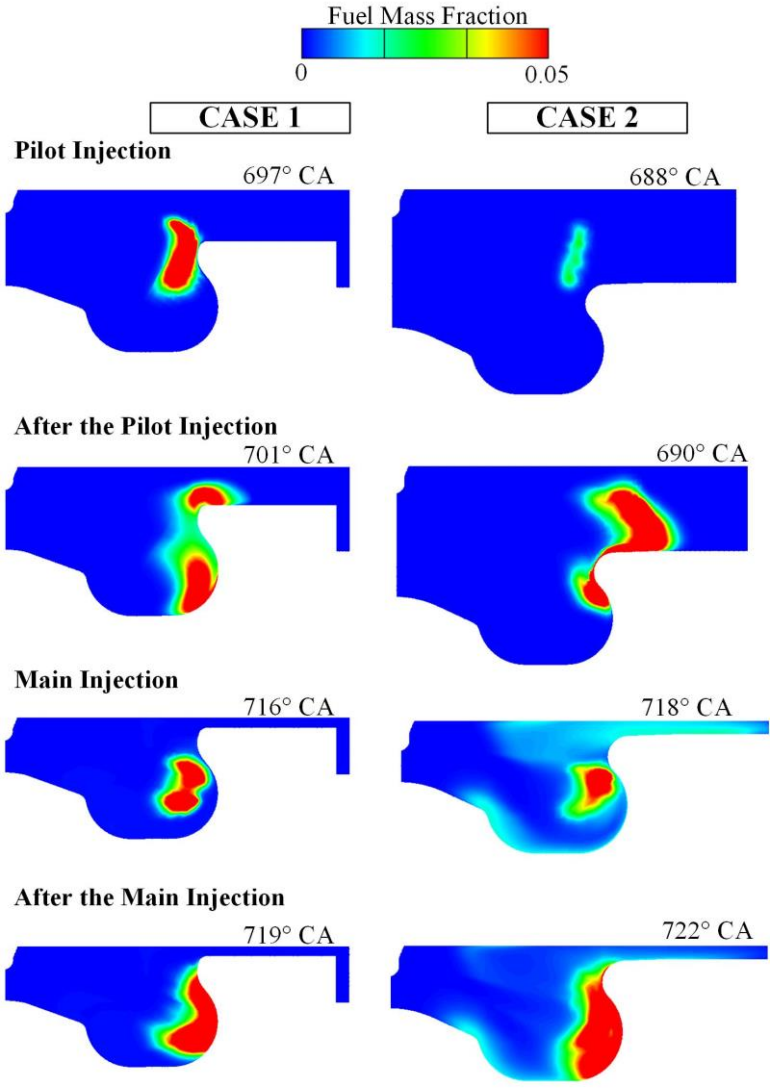

Figure 45 Comparison of evaporated fuel in Case 1 and 2

6. CONCLUSION

In this work, the 3D Computational Fluid Dynamics (CFD) software AVL FIRE® was used to model the experimental engine. The first step in this work was to examine the dependency of the simulation results on some not known input parameters. The impact of swirl motion inside the cylinder on the in-cylinder pressure was tested. The presented results in chapter 5.1. show that the impact of the swirl on the in-cylinder pressure could be neglected. But for the other results, e.g. the emission results, the swirl motion inside the cylinder has to be considered. The influence of the multi-injection on results was examined shifting the total mass between the injections. The impact of the mass distribution on pressure results has significant influence with changing only 10 percent of the input value. The multi-injection systems require much experimental work to evaluate the effect of each single parameter, so the development of CFD simulation for multi-injection systems can be an alternative. The most significant impact on 2D results has the spray sub-model, especially the C_2 constant in selected WAVE breakup model, which determines the breakup time of droplets. Due to that, the constant C_2 was variable with the time. The comparison between two operating cases with the same parameters did not present connection between 3D results of those two cases. Due to fuel droplet parcels in compensation volume for operating case 2. Impacts of all those parameters made this work very case-dependent.

The objective of this work was also a comparison of the numerical results with the experimental data. For the final results, the comparison between the combustion model and the chemical mechanism (n-heptane) showed the deviation, due to different fuel characteristics. Numerous simulations were calculated to test the influence of a lot of different parameter on 2D results. To understand the influence of every parameter and to avoid the misinterpretation, the 3D results had to be analysed. A lot of criteria for 2D were obtained from analysing 3D results. In this work, Euler Lagrangian model was used for the spray modelling. In the future, the idea is to test the Euler Eulerian approach in spray modelling, due to its better accuracy at near nozzle flow.

REFERENCES

[1] http://www.iea.org/ , last access 26.11.2016.

[2] https://www.fuelseurope.eu/knowledge/how-refining-works/diesel-gasoline-imbalance/ , last access 26.11.2016.

[3] Petranović Z.: Numerical Modelling of Spray and Combustion Processes using the Euler Eulerian Multiphase Approach, Doctoral Thesis, FSB, 2016

[4] Pulkrabek W. W.: Engineering Fundamentals of the Internal Combustion Engine, Pearson Education Limited, Edinburgh, 2014

[5] http://www.hk-phy.org/energy/transport/vehicle_phy01_e.html , last access 26.11.2016

[6] Stone R.: Introduction to Internal Combustion Engines, MacMillan Press Ltd., London, 1999

[7] Galović A.: Termodinamika 1, FSB, Zagreb 2011.

[8] http://hyperphysics.phy-astr.gsu.edu/hbase/thermo/diesel.html , last access 26.11.2016

[9] Heywood J. B.: Internal Combustion Engine Fundamentals, McGraw-Hill, Inc., New York, 1990

[10] Rajput R. K.: Thermal Engineering, Laxmi Publication, Boston, 2010

[11] Vujanović M.: Numerical Modelling of Multiphase Flow in Combustion of Liquid Fuel, Doctoral Thesis, FSB, 2010

[12] Poinsot T., Veynante D.: Theoretical and Numerical Combustion, Edwrads, 2012

[13] Laramee R. S., Garth C., Schneider J., Hauser H.: Texture Advection on Stream Surfaces: A Novel Hybrid Visualization Applied to CFD Simulation Results, Jan 2006

[14] Moufalled F., Mangani L., Darwish M.: The Finite Volume Method in Computational Fluid Dynamics, Springer, 2015

[15] Warnatz J., Maas U., Dibble R. W.: Combustion, Springer, 2006

[16] AVL FIRE® Version 2014.2 Manual: Combustion Module, Graz, 2016

[17] Hanjalic, K., Popovac, M., Hadziabdic, M.: A robust near-wall elliptic relaxation eddy viscosity turbulence model for CFD, 2004

[18] Zhao, H.: Advanced direct injection combustion engine technologies and development, Woodhead Publishing Limited, Oxford, 2010.

[19] Baleta J..: Development of Numerical Models within the Liquid Film and Lagrangian Spray Framework, Doctoral Thesis, FSB, 2016

[20] AVL FIRE® Version 2014.2 Manual: Spray Module, Graz, 2016

[21] Jafarmadar S., Khanbabazadeh M.: A Full-Cycle 3 Dimensional Numerical Simulation Of a Direct Injection Diesel Engine, International Journal of Automotive Engineering, Vol. 3, Number 2, June 2013, pp. 424 - 434

[22] Liu A. B., Mather D., Reitz R. D.: Modeling the Effects of Drop Drag and Breakup on Fuel Sprays, SAE Technical Paper Series, Detroit 1993.

[23] Dukowicz J. K.: Quasi-steady droplet phase change in the presence of convection, Los Almos Scientific Laboratory, 1979.

[24] Chung T. J.: Computational Fluid Dynamics, Cambridge University, 2002.

[25] Patankar V. S.: Numerical Heat Transfer and Fluid Flow, Hemisphere publishing corporation, Washington, 1980

[26] Kenneth K. : Fundaments of turbulent and multiphase combustion, Wiley, New Jersey, 2005.

ATTACHMENTS

1. CD-R disc